JGR Space Physics

RESEARCH ARTICLE
10.1029/2023JA031656

Identifying the Variety of Jovian X-Ray Auroral Structures: Tying the Morphology of X-Ray Emissions to Associated Magnetospheric Dynamics

D. M. Weigt[1,2,3], C. M. Jackman[2], D. Moral Pombo[4], S. V. Badman[4], C. K. Louis[2], W. R. Dunn[5], S. C. McEntee[2,3], G. Branduardi-Raymont[6], D. Grodent[7], M. F. Vogt[8], C. Tao[9], G. R. Gladstone[10], R. P. Kraft[11], W. S. Kurth[12], and J. E. P. Connerney[13,14]

[1]School of Physics and Astronomy, University of Southampton, Southampton, UK, [2]School of Cosmic Physics, DIAS Dunsink Observatory, Dublin Institute for Advanced Studies, Dublin, Ireland, [3]School of Physics, Trinity College Dublin, Dublin, Ireland, [4]Department of Physics, Lancaster University, Lancaster, UK, [5]Department of Physics and Astronomy, University College London, London, UK, [6]Mullard Space Science Laboratory, University College London, Dorking, UK, [7]Laboratory for Planetary and Atmospheric Physics, Space Science, Technologies and Astrophysical Research Institute, University of Liège, Liège, Belgium, [8]Center for Space Physics, Boston University, Boston, MA, USA, [9]National Institute of Information and Communications Technology, Tokyo, Japan, [10]Southwest Research Institute, San Antonio, TX, USA, [11]Harvard-Smithsonian Center for Astrophysics, Smithsonian Astrophysical Observatory, Cambridge, MA, USA, [12]Department of Physics and Astronomy, University of Iowa, Iowa City, IA, USA, [13]Space Research Corporation, Annapolis, MD, USA, [14]NASA Goddard Space Flight Center, Greenbelt, MD, USA

Abstract We define the spatial clustering of X-rays within Jupiter's northern auroral regions by classifying their distributions into "X-ray auroral structures." Using data from Chandra during Juno's main mission observations (24 May 2016 to 8 September 2019), we define five X-ray structures based on their ionospheric location and calculate the distribution of auroral photons. The morphology and ionospheric location of these structures allow us to explore the possibility of numerous X-ray auroral magnetospheric drivers. We compare these distributions to Hubble Space Telescope (HST) and Juno (Waves and MAG) data, and a 1D solar wind propagation model to infer the state of Jupiter's magnetosphere. Our results suggest that the five sub-classes of "X-ray structures" fall under two broad morphologies: fully polar and low latitude emissions. Visibility modeling of each structure suggests the non-uniformity of the photon distributions across the Chandra intervals are likely associated with the switching on/off of magnetospheric drivers as opposed to geometrical effects. The combination of ultraviolet (UV) and X-ray morphological structures is a powerful tool to elucidate the behavior of both electrons and ions and their link to solar wind/magnetospheric conditions in the absence of an upstream solar monitor. Although much work is still needed to progress the use of X-ray morphology as a diagnostic tool, we set the foundations for future studies to continue this vital research.

Plain Language Summary The mechanism that allows precipitation of ions into Jupiter's atmosphere and generate pulsed X-ray auroral emissions is still under debate today. Previous studies have linked this driver to possible activity in Jupiter's outer magnetosphere (the interface between the solar wind and Jupiter) and have observed the emissions to exhibit variable behavior. More recent studies have suggested a wide range of physical phenomena causing these emissions. Here we explore this idea in more detail by introducing five "X-ray auroral structures" that map to different regions in the Jovian system. Using data from the Chandra X-ray Observatory during Juno's main mission allows us to calculate the distribution of X-rays from Jupiter's northern auroral region. We compare our X-ray results with the ultraviolet emissions ("UV auroral families") observed from simultaneous Hubble Space Telescope (HST) data and infer the conditions at Jupiter using models and Juno observations. These "X-ray structures" provide us with many ways to observe variable behavior and provide a possible tool to monitor the solar wind conditions, when used in tandem with the HST "UV auroral families."

Key Points:

- We present the morphology of new "X-ray auroral structures," observed on Jupiter via Chandra's high spatial resolution camera
- We show that non-uniform auroral photon distributions are likely from "switching on/off" of auroral driver(s) opposed to planetary tilt
- We show that combination of X-ray and ultraviolet (UV) "auroral families" may be a useful proxy to determine the magnetospheric conditions at Jupiter

Supporting Information:

Supporting Information may be found in the online version of this article.

Correspondence to:

D. M. Weigt,
dale.weigt@aalto.fi

Citation:

Weigt, D. M., Jackman, C. M., Moral Pombo, D., Badman, S. V., Louis, C. K., Dunn, W. R., et al. (2023). Identifying the variety of Jovian X-ray auroral structures: Tying the morphology of X-ray emissions to associated magnetospheric dynamics. *Journal of Geophysical Research: Space Physics*, *128*, e2023JA031656. https://doi.org/10.1029/2023JA031656

Received 28 APR 2023
Accepted 17 OCT 2023

Author Contributions:

Conceptualization: D. M. Weigt, C. M. Jackman, D. Moral Pombo, S. V. Badman, W. R. Dunn, S. C. McEntee, D. Grodent, C. Tao, G. R. Gladstone, W. S. Kurth
Data curation: D. M. Weigt, C. M. Jackman, D. Moral Pombo, S. V. Badman, C. K. Louis, W. R. Dunn, S. C. McEntee, G. Branduardi-Raymont, G. R. Gladstone, R. P. Kraft, W. S. Kurth

1. Introduction

The Jovian auroral emissions are very complex and are highly variable in their morphological and temporal behavior across multiple wavelengths (see full review by Badman et al. (2015) and references therein for more details). The X-ray emissions remain the most elusive of the observable aurora with many recent studies trying to

Formal analysis: D. M. Weigt, C. M. Jackman, D. Moral Pombo, S. V. Badman, C. K. Louis, W. R. Dunn, S. C. McEntee, G. Branduardi-Raymont, C. Tao, G. R. Gladstone, R. P. Kraft, W. S. Kurth
Funding acquisition: C. M. Jackman, S. V. Badman, W. R. Dunn, G. Branduardi-Raymont, C. Tao, W. S. Kurth
Investigation: D. M. Weigt, C. M. Jackman, D. Moral Pombo, S. V. Badman, C. K. Louis, W. R. Dunn, S. C. McEntee, G. Branduardi-Raymont
Methodology: D. M. Weigt, C. M. Jackman, D. Moral Pombo, S. V. Badman, C. K. Louis, W. R. Dunn, S. C. McEntee, G. Branduardi-Raymont, D. Grodent, G. R. Gladstone, W. S. Kurth
Project Administration: D. M. Weigt, C. M. Jackman
Resources: D. M. Weigt, D. Moral Pombo, S. V. Badman, C. K. Louis, W. R. Dunn, S. C. McEntee, D. Grodent, M. F. Vogt, C. Tao, W. S. Kurth, J. E. P. Connerney
Software: D. M. Weigt, D. Moral Pombo, S. V. Badman, C. K. Louis, W. R. Dunn, S. C. McEntee, G. R. Gladstone
Supervision: C. M. Jackman, S. V. Badman
Validation: D. M. Weigt, C. M. Jackman, S. V. Badman, W. R. Dunn, S. C. McEntee, G. Branduardi-Raymont, W. S. Kurth
Visualization: D. M. Weigt, D. Moral Pombo, S. V. Badman, C. K. Louis
Writing – original draft: D. M. Weigt
Writing – review & editing: D. M. Weigt, C. M. Jackman, D. Moral Pombo, S. V. Badman, C. K. Louis, S. C. McEntee, G. Branduardi-Raymont, D. Grodent, M. F. Vogt, C. Tao, R. P. Kraft, W. S. Kurth, J. E. P. Connerney

understand the highly sophisticated magnetospheric driver(s) capable of energizing the ions to MeV energies that allow charge stripping and charge exchange to take place in the Jovian ionosphere for soft X-ray (SXR: <1 keV) production (e.g., Dunn et al., 2020a, 2020b; Houston et al., 2020). The SXRs are produced from precipitating MeV ions originating in the outer magnetosphere and are sometimes observed to be coincident with flaring ultraviolet (UV) emissions within the UV active polar region as observed by Dunn et al. (2022) (herein refereed to as D22). The auroral hard X-rays (HXR: >2 keV) result from bremsstrahlung emissions from precipitating electrons, with the auroral emissions observed to sometimes coincide with the UV main emission (ME: e.g., Branduardi-Raymont et al., 2008; Dunn et al., 2016). This suggests that the precipitating electrons responsible for the HXR and UV ME auroral emissions are likely to originate in the same region of the middle magnetosphere. Recent and ongoing studies are investigating how the X-rays are connected to other auroral emissions in the EM spectrum via plasma waves such as electromagnetic ion cyclotron (EMIC) waves associated with precipitating ions, which are shown to be strongly correlated with X-ray pulsations for example, Yao et al. (2021). Other studies have looked at how the HXR are correlated with the more intense UV auroral emissions (Wibisono et al., 2021), such as dawn storms—major enhancements of the UV ME along the dawn arc with a broadening in latitude (Bonfond et al., 2021; Yao et al., 2020).

Previous studies analyzing the Jovian UV aurorae from the Hubble Space Telescope (HST) have isolated various regions within the auroral emissions to explore the temporal and morphological variation across them. Nichols et al. (2009) used data from two 2007 HST campaigns to identify three northern UV auroral components: (a) the main oval (ME), (b) low-latitude and (c) high-latitude auroral emissions. They calculated the auroral power, via analysis of the observations and visibility modeling of each region, and predicted solar wind conditions propagated from Earth to investigate the most likely cause of variation. Their results showed that generally the auroral power from the polar regions (low- and high-latitude auroral emissions) were uncorrelated with that of the ME unless a dawn storm or enhancements due to a magnetospheric compression occurred. This may be a result of the polar emissions, in particular the swirl region observed to contain patchy and turbulent auroral emissions at the center of the UV polar auroral emissions, having a strong local time dependence (Greathouse et al., 2021).

Nichols et al. (2017) followed up their previous study by segmenting the northern auroral region further, focusing on four regions of interest. These regions were applied to a larger HST data set (around 47 orbits in total), covering May–July 2016 during Juno's (Bolton et al., 2017) final approach to Jupiter and its orbit insertion in the dawn flank of Jupiter's magnetosphere. By comparing the Juno in situ interplanetary data (McComas et al., 2017) and the HST UV auroral images they observed the intensity of the ME (at System III [SIII] longitudes >170°) to increase for 1–3 days following compression events identified by Juno, with emissions on the polar dusk side to also brighten during these times and during shallow rarefactions of the solar wind. Auroral emissions equatorward of the ME (at SIII longitudes <190°) brightened ∼10 days following enhanced Io plasma torus emissions observed from the EXtreme ultraviolet spetrosCope for ExosphEric Dynamics on board Hisaki (Yoshioka et al., 2013). The noon active region did not show any clear correlation between intensity and interplanetary conditions, although the morphology was observed to change between periods of rarefactions and compressions. The variability of these emissions across the specific regions highlights how the auroral and magnetospheric dynamics change across different local times.

More recently, Grodent et al. (2018) (herein referred to as G18) characterized 118 HST images during Juno orbits 3–7 (from 30 November 2016 up to and including 18 July 2017), using six new definitions of "UV auroral families" to help provide a simplified description of the complex dynamics observed in the UV auroral emissions: (a) *Q* (or "quiet") has a very low auroral power (<1 TW) with a lower latitude ME; (b) *N* has a "narrow" and expanded ME, exhibiting average power; (c) *U* describes more "unsettled" conditions and is the intermediate behavior between *Q* and *N*; (d) *I* is associated with strong injections with a "corner-like" morphology, located at ionospheric dusk with (e) more moderate injections being represented by the *i* family. (f) The final family, *X*, is linked to "eXternal" perturbations generating very strong and contracted ME with large enhancements at dawn and strong, narrow auroral arcs in the afternoon-dusk sector. Such behavior is usually observed during solar wind compressions. These new definitions allowed different morphologies to be compared to establish logical, plausible connections to identify the responsible auroral driver and allowed a more detailed quantitative way to analyze variations of spatial behavior. G18 observed that auroral emissions corresponding to the *U* family occurred most often (29.5% of 118 HST images) and were identified to be connected to the *Q* family due to slight changes in brightness of the ME. The connection was only interrupted by episodes of injection events (*I, i*) which were observed to precede or follow the *N* family. The moderate injections, *i*, were identified after auroral structures

associated with compressions of the interplanetary medium (*X*). This was verified by a recent study by Yao et al. (2022) who found systematic evidence linking "main auroral brightenings" (MABs: brightening of the ME at all local times within HST's field of view) to compression events found by Juno. The MABs were observed to correspond with the *I* and *X* UV families, emphasizing the robustness of using auroral morphologies as an indicator of magnetospheric dynamics. The disturbances from compressions can trigger episodic injections of trapped particles in the middle magnetosphere, as observed by Louarn et al. (2014) from Galileo particle and radio measurements. More details of the UV auroral families described here can be found in G18. Yao et al. (2020) found that dawn storms and injection events were correlated with intervals of tail reconnection and dipolarization.

In this study, we utilize the techniques used for the UV auroral emissions to isolate and define specific auroral structures and apply them to the concentrated northern X-ray emissions in an attempt to find a link between X-ray morphology and magnetospheric dynamics. We use concurrent HST data to help provide vital magnetospheric context to the Chandra (Weisskopf et al., 2000) observations, using the G18 auroral definitions, and model the visibility of the X-ray auroral structures we define here, similar to Nichols et al. (2009). We then compare the magnetospheric dynamics found from the X-ray-UV data and compare with the magnetospheric conditions identified from the Juno spacecraft, using radio (Kurth et al., 2017) and magnetometer (Connerney et al., 2017) data. This allows us to determine the state of the Jovian magnetosphere and to compare against the solar wind predictions of the Tao et al. (2005) 1D magnetohydrodynamic (MHD) solar wind propagation model. Similar to the logic applied by G18, the goal of this study is to simplify the complex morphological variations of the X-ray aurora, allowing plausible connections to be made between the auroral emissions and magnetospheric dynamics. Linking our X-ray structures with the UV equivalent may provide additional context from which to infer the state of the Jovian magnetosphere in the absence of upstream solar wind data.

Previous observations noted morphological variations in the X-ray aurora and attempted to connect this with solar wind conditions for a limited sample of observations taken in 2007 and 2011, for which interpretation was further challenged by limitations on viewing geometry (Dunn et al., 2016, 2020a, 2020b). The work here, with a more comprehensive observation data set supported by in situ insights from the Juno spacecraft, may also help to put these historic X-ray observations into context.

2. Contemporaneous Remote Sensing UV and X-Ray Observations With Juno Waves and MAG Data

We use the catalog of Chandra HRC-I (High Resolution Camera—Imaging: 30 × 30 arcmin field of view, with pixel size 0.13 arcsec and spatial resolution of 0.4 arcsec) observations defined and tabulated in Weigt et al. (2021c), with the fully processed data sets provided by Weigt et al. (2021b), focusing on those taken during the Juno main mission (24 May 2016 up to and including 8 September 2019). The Chandra observations used here are a combination of HXRs and SXRs due to the very limited spectral resolution of HRC-I, meaning that we cannot segregate photons of these two energy regimes. However, previous work suggested that greater than 90% of the observed X-ray photons detected by Chandra Advanced CCD Imaging Spectrometer (ACIS) were soft X-ray photons (Dunn et al., 2020a) and the energy response of HRC is softer than ACIS, so that we expect the majority of detected X-ray photons to be produced by precipitating ions. These observations include those taken during Juno's approach to Jupiter (in the solar wind), while Juno was at apojove (near the dawn magnetopause), during several perijoves and intervals when Juno was inside and crossed the Jovian plasmasheet. We then correct the Chandra observations using the updated mapping algorithm (assuming the altitude of X-ray emissions is 400 km above the 1-bar atmosphere) described in McEntee et al. (2022), to account for the decreasing HRC gain and instrument degradation over time. This consists of applying a multiplicative gain correction factor to the X-ray signal to convert the distribution as if it were unaffected by these issues (i.e., correct the distribution as if it were observed in the year 2000, when the gain was stable). Using this new distribution, known as the Pulse Invariant (PI) distribution, we select the PI channel range where the source signal dominates the background and remove any other instrumental effects (e.g., potential build-up of instrumental noise). Using the fact that Jupiter occults any X-rays that may be behind it and the position of the planet on the detector, we can select the planet-sized region such that much of the remaining background is removed and that we only analyze Jovian photons (McEntee et al., 2022; Weigt et al., 2022). Here our focus is on the brightest and most concentrated X-ray northern auroral emissions, located using the Weigt et al. (2020) numerical criterion of >7 photons per 5° SIII longitude × 5° latitude over ∼10 hr (the average duration of the observations of the catalog, around a

Jovian rotation). As the Jovian auroral emissions are far more concentrated than the background signal, our signal-to-noise improves further. We note using this more updated mapping method provides minimal change in X-ray count rates from the Weigt et al. (2021c) study and therefore does not change the interpretation of these results. We highlight here that accounting for the instrument's increasing degradation (and particle background) is crucial for future studies during the Juno extended mission (especially when mapping X-ray emissions to the Jovian disk). The degradation of HRC-I has also been observed when analyzing time-tagged photon data in a low-count regime from Saturn (Weigt et al., 2021a).

To help provide essential magnetospheric context to the X-ray auroral emissions, we use HST observations concurrent with Chandra data. We analyze 17 Chandra observations in total during the Juno-era. Of these, 14 have HST Space Telescope Imaging Spectrograph (STIS: 24.7 × 24.7 arcsec field of view, spatial resolution of 0.025 arcsec) data ±1 day from the Chandra window, to allow the magnetospheric conditions to be analyzed in detail. These 14 Chandra observations with HST orbits are displayed in Table 1. The exception being Observation ID (ObsID) 20002 (6 August 2017) which had no simultaneous HST observations within the ±1 day interval but is during an inferred compression event from Juno, bringing the number of tabulated Chandra observations to 15. STIS detects far ultraviolet auroral emissions of wavelengths ∼130–180 nm (photon energies ∼7–10 eV) using the F25SRF2 filter to eliminate geocoronal Ly-α contamination and to reduce the reflected sunlight from the Jovian disk (e.g., Grodent, 2015). These 14 HST observations focus on the northern auroral emissions of which components within the UV aurora have been identified using the G18 definitions. We note that we add to this catalog with three newly identified HST observations coinciding with ObsID 22159 (29 May 2019), 22150 (18 June 2019) and 22151 (8 September 2019). All observations used in this research are shown in Table 1. To compare with contemporaneous Juno data, both the Chandra and HST intervals have been corrected for the Juno-Earth light-travel time, taken from ephemeris data obtained via the JPL Horizons database (data available at https://ssd.jpl.nasa.gov/horizons/app.html#). The mean and max dynamic pressure (P_{dyn}) estimated from the Tao et al. (2005) 1D MHD model over a 2 days window centered on the Chandra interval with the corresponding average Jupiter-Sun-Earth (JSE) angle are also given in Table 1. This 2-day window is used for all observations irrespective of JSE angle to account for propagation and interpolation errors. We note that Chandra observations taken beyond 8 September 2019 (and after the creation of the Weigt et al. (2021c) catalog) have no direct overlap with any HST campaigns and are therefore not included in this study.

We then compare these observations to remote sensing radio data (spectrograms) from Juno Waves and in situ data (time series) from the magnetometer, Juno MAG to confirm the magnetospheric state during these intervals and potentially identify any internal magnetospheric drivers (e.g., such as particle injection signatures). Juno's eccentric polar orbit allows it to sample the inner, middle and outer magnetosphere during its 53-day orbit, providing us the opportunity to analyze the different internal auroral drivers, hence the auroral emissions, located throughout the Jovian magnetosphere. We take this into account when interpreting these data.

3. Results

Following studies that have identified different regions within the UV emissions associated with different potential drivers (e.g., Grodent et al., 2018), we apply similar logic to the X-ray northern auroral emissions from the Weigt et al. (2021c) Chandra catalog during the Juno-era. Here we use the families defined from UV emissions from concurrent HST observations to provide vital context to the concentrated northern X-ray emissions and use the superior spatial resolution of HST-STIS to model the visibility of each X-ray auroral region. All data sets created in this study (i.e., coordinates of X-ray auroral structures, PI filtered time-tagged photon lists, visibility modeling) and used throughout this study (main text and any Supporting Information S1) can be found in Weigt et al. (2023).

3.1. Identifying X-Ray Auroral Structures

As analyzed in the statistical study by Weigt et al. (2021c), it is clear that the northern X-ray emissions exhibit large variations in morphological and temporal behaviors with only a very small region of X-rays appearing across the entire ∼20 years Chandra HRC-I data set: the averaged hot spot nucleus (AHSNuc), mapping to the noon magnetopause boundary. We show examples of 2D histograms of mapped concentrated X-rays, using the Weigt et al. (2020) numerical criterion, in Figure 1 within the *X-ray noon* region (red), where the color bar

Journal of Geophysical Research: Space Physics
10.1029/2023JA031656

Table 1
Table of Concurrent Chandra and Hubble Space Telescope (HST) Observations Throughout the Juno Era

Observation start date (dd/mm/yyyy)	Chandra ObsID	Observation interval (Juno time; light corrected)		HST UV northern auroral family[a]			Mean solar wind[b] P_{dyn} (nPa)	Max solar wind[b] P_{dyn} (nPa)	Mean Jupiter-Sun-Earth angle[b] (°)
		Chandra	HST	G18[c]	This study	D22[d]			
24/05/2016	18608	09:39–20:41	17:03–17:47	–	U	Q/N	0.006	0.007	~57.7
			20:14–20:58	–	U	U			
01/06/2016	18609	10:47–21:49	14:13–14:57	–	U	Q/N	0.138	0.309	~64.6
			17:24–18:08	–	U	Q/N			
02/02/2017	18301	09:14–18:19	16:17–16:57	–	i	i	0.009	0.015	~−79.9
28/02 (Chandra); 01/03/2017 (HST)[e]	20000[e]	11:58–07:34	14:37–15:16	i	i	–	0.019	0.024	~−53.3
18/05–19/05/2017	18302	23:48–10:10	04:27–05:07	N	N	N	0.052	0.148	~19.2
			06:03–06:43	N	N	N			
18/06/2017[e]	**20001**[e]	**17:55–04:06**	**08:31–09:13**	**X**	**i**	–	**0.090**	**0.230**	**~47.9**
06/08/2017[f]	20002[f]	01:07–10:50	–	–	–	–	0.015	0.024	~99.0
01/04/2018	**18678**	**09:59–21:06**	**09:59–10:17**	–	**X**	–	**0.116**	**0.275**	**~−58.4**
23/05–24/05/2018	18679	23:22–10:21	09:02–09:32	–	U	Q	0.049	0.115	~−3.6
06/09/2018	**18680**	**19:50–06:56**	**04:22–05:02**	–	**i**	**X**	**0.056**	**0.086**	**~97.0**
29/05/2019	22159	02:50–12:34	12:18–12:56	–	i	–	0.014	0.019	~−32.5
15/07/2019	22148	12:21–19:13	14:06–14:44	–	U	N	0.068	0.115	~10.5
			15:41–16:17	–	U	Q			
16/07/2019	22149	08:07–15:00	10:43–11:21	–	N/i	N	0.057	0.096	~11.3
18/07/2019[e]	22150[e]	19:40–01:32	14:10–14:49	–	i	–	0.012	0.018	~13.9
08/09/2019	**22151**	**08:01–14:46**	**14:24–15:02**	–	**X/i**	–	**0.262**	**0.879**	**~64.0**

Note. Date and time of each observation, identified UV auroral families from current literature using the G18 definition and predicted solar wind dynamic pressure from the Tao et al. (2005) model with average Jupiter-Sun-Earth angle are shown. Bold entries highlight observations associated with possible eXternal perturbation (X) structures linked with potential compression events as confirmed by Yao et al. (2022). Solar wind parameters determined over a 2 days window centered on the Chandra observation to account for propagation errors within Tao et al. (2005) model. Each Chandra observation is labeled with a unique Observation ID (ObsID).

[a]UV families as described in Grodent et al. (2018). [b]Predicted values from Tao et al. (2005) model over 2 days window centered on Chandra observation. [c]UV families identified from Grodent et al. (2018) (G18). [d]UV families identified from Dunn et al. (2022) (D22). [e]Observations not concurrent but occurred ±1 day from Chandra interval. [f]Inferred compression from Juno data, no HST data.

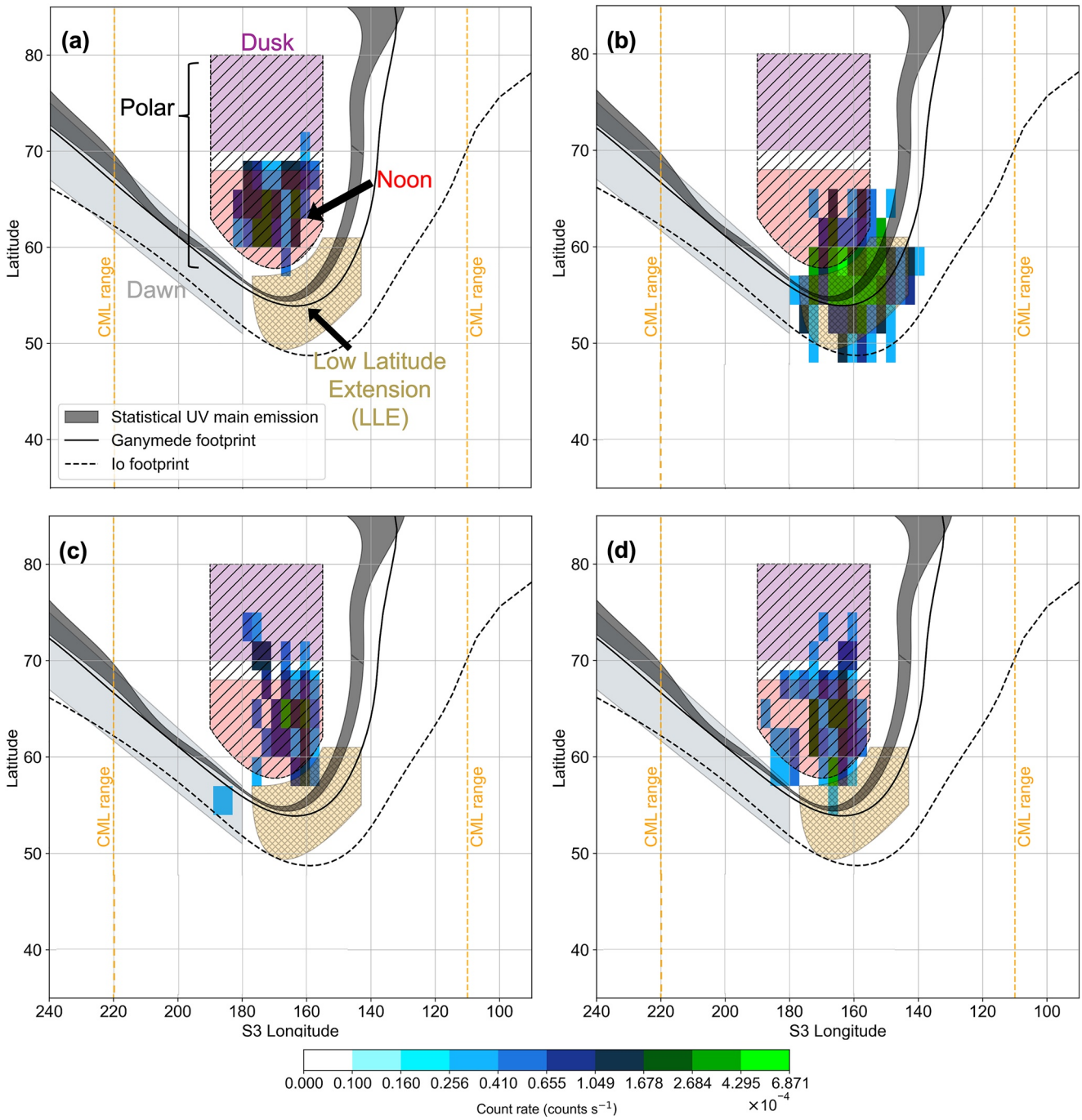

Figure 1. A Cartesian plot of the X-ray mapping for four example Chandra observations analyzed in this research, each under different conditions: (a) Observation ID (ObsID) 18301 (2 February 2017), where all auroral emissions are within the polar region; (b) ObsID 22151 (8 September 2019), where the auroral emissions are shifted equatorward and two cases linked to *X*-family ultraviolet (UV) emissions during (c) a confirmed compression event (ObsID 20001: 18 June 2017) and (d) a potential compression event (ObsID 18678: 1 April 2018) during a Juno perigee (or perijove), where we are unable to infer the magnetospheric state from using Juno data alone. Each case is expanded upon in the remainder of Section 3. The location of the X-ray auroral structures as described in the text (red: noon; purple: dusk; gray: dawn; gold: LLE; striped: polar) are shown in each panel and are labeled in (a). The count rates (counts s^{-1}) of the concentrated X-ray auroral emissions (2D histogram: binned by 3° SIII lon × 3° lat) are given by the color bar. The statistical UV main emission accounting for compressed and expanded states (dark gray shading; Bonfond et al., 2017), and the JRM33 magnetic footprints of Io (black-dashed line) and Ganymede (solid black line) are overplotted (Connerney et al., 2020, 2022). The X-ray emissions mapped and analyzed for this research are selected from a 9,000 ± 1,080 s interval, covering a central meridian longitude (CML) range of 110°–220° (i.e., optimum visibility for each region as shown in Figure S3 in Supporting Information S1). This CML range is overplotted with orange dashed lines.

shows the photon flux of the X-rays (counts s^{-1}; calculated over an interval of ~Jovian rotation, with concentrated photons selected that follow both numerical and central meridian longitude [CML] criteria). Similar to the "Region X" defined in D22, the X-ray noon region contains both the UV swirl and active regions (Grodent, Clarke, Waite et al., 2003) and therefore the X-ray emissions they may generate. We do emphasize that although this research is complementary to D22, the main science question in both studies are different. D22, as mentioned, focuses on finding the existence of a dark polar region (DPR) equivalent in the X-ray aurora and focuses on remote sensing data. Here, we are focused on using a combination of X-ray and UV morphologies as a possible indicator of magnetospheric conditions at Jupiter, from available Juno data, in the absence of an in situ solar wind upstream monitor. Therefore, our study follows up on D22's results by expanding the analysis to the full X-ray northern auroral region and compares it to other data sets and models.

The remaining X-ray auroral structures we define here are *X-ray dusk* (purple), *X-ray dawn* (gray), the *Low Latitude Extension region* (LLE; gold), equatorward of X-ray noon and the *X-ray polar region* (striped region) which envelopes both the noon and dusk structures. The statistical UV ME (accounting for a compressed and expanded magnetosphere) from Bonfond et al. (2017) and Io and Ganymede magnetic footprints from JRM33 (Connerney et al., 2022) with the Connerney et al. (2020) magnetodisc model are also plotted to provide context of the location of these regions within the magnetosphere. The coordinates of each region (in SIII lon, lat) are given in Supporting Information S1 (see Data Set S1). We note that these UV reference features used to provide context to the X-ray auroral structures vary with CML (e.g., Grodent, Clarke, Kim et al., 2003; Vogt et al., 2022).

In Figure 1 (covering a wide range of CMLs: 110°–220° or a time interval of 9,000 ± 1,080 s [equivalent to ~2.5–3 hr]), we show four examples of different auroral morphologies each under different conditions: (a) where all auroral emissions are within the polar region (ObsID 18301: 2 February 2017); (b) where the most intense auroral emissions are observed to be shifted equatorward (ObsID 22151: 8 September 2019) and two cases of auroral morphology associated with *X*-family UV emissions during (c) a confirmed compression event (ObsID 20001: 18 June 2017) and (d) a potential compression event (ObsID 18678: 1 April 2018). Panel (d) shows an observation observed during a Juno perigee (or perijove), where we are unable to infer the magnetospheric state from using Juno data alone. Both (c) and (d) exhibit fairly similar morphologies, potentially showing signs of similar magnetospheric states. These individual cases are discussed in greater detail in Section 3.3, using UV and X-ray morphologies to infer the state of the magnetosphere.

Three out of the four cases show the majority of the concentrated, and most intense, X-ray emissions are located in the X-ray polar region, dominated by X-ray noon. These emissions are therefore likely to be co-located (and possibly linked) with the UV activity in the polar and swirl regions and possibly coincide with flaring UV emissions (e.g., Dunn, 2022; Elsner et al., 2005). Previous studies (e.g., Grodent, 2015; Grodent, Clarke, Waite et al., 2003; Greathouse et al., 2021) and references therein) have also identified the polar active region as the most dynamic of the UV polar emissions, producing flares and bright arc sub-structures of a few hundred kilo-Rayleigh (kR) lasting in the order of a few minutes. The examples shown in Figure 1 are discussed further in the remainder of Section 3.

The X-ray dawn region is found to coincide with a portion of the ME and the Io footprint suggesting an association between dawn storms, injections of hot plasma from the middle magnetosphere (e.g., Gerard et al., 1994; Kimura et al., 2017) and bright X-ray populations. Recent work by Wibisono et al. (2021) found the intensity of the HXRs to increase during the presence of a dawn storm with reduced activity from the more poleward SXRs, utilizing the energy resolution of XMM-Newton. Dawn storms typically have a duration of at least 1–2 hr (e.g., Ballester et al., 1996), therefore our CML thresholding (spanning an interval of 2.5–3 hr during each Chandra observation) will be sufficient to detect the brightest signatures associated with these events, if any. Regions of X-ray dawn at higher latitudes are likely to overlap with the UV DPR which contains very little UV emissions and is observed to contract and expand as Jupiter rotates, mapping to the outer magnetosphere (e.g., Grodent, Clarke, Waite et al., 2003; Pallier & Prangé, 2001; Swithenbank-Harris et al., 2019). The DPR has been found to be the likely location of empty flux tubes, emptied via Vasyliūnas-like reconnection in the tail which then rotate to the dayside magnetosphere (Vasyliūnas, 1983), resulting in very little UV emissions here. Recent work by D22 found that the DPR is also present within the X-ray northern auroral emissions. D22 deduced from Chandra and HST observations (and simulated data) that very few or no X-ray photons are to be located in the DPR. They confirm this conclusion from their Monte Carlo simulations which state that the likelihood of X-rays being emitted from the DPR is very small, including possible scattering of solar X-ray photons in the Jovian upper atmosphere as an explanation for the sporadic and very dim X-ray emissions in the Dark region.

The regions likely to contain more extreme cases of auroral activity are the X-ray dusk (see Figures 1c and 1d) and LLE regions (Figure 1b) where the brightest emissions may span poleward or equatorward of the nominal position as found by Weigt et al. (2021c), where it was observed that concentrated X-ray photons are occasionally (30%–70% occurrence) found at latitudes between 54° and 75°. Therefore these regions will likely contain rare auroral morphologies linked to more unusual and extreme magnetospheric dynamics or those events that have a long travel time to the Jovian ionosphere (e.g., signatures from possible tail reconnection). The X-ray dusk region is situated at higher longitudes, and is likely the location for auroral emissions associated with processes in the magnetotail such as possible midnight spots linked to tail reconnection. These UV features have been observed to generate auroral power of several gigawatts (e.g., Kasahara et al., 2013; Radioti et al., 2011). Such emissions result from the precipitation of heated plasma from tail reconnection as a consequence of inward moving plasma flow being released at these sites. The LLE region covers an area of UV auroral emissions possibly associated with active particle injections from the middle magnetosphere driven by reconnection events and dipolarizations of the Jovian magnetic field (e.g., Dumont et al., 2014, 2018; Yao et al., 2020). Such injection events are found to occur alongside dawn storms, suggesting disturbances of the middle magnetosphere at a range of local times (e.g., Gray et al., 2016). The 2-D histograms for all observations analyzed and corresponding plots highlighting the filtering performed on the concentrated X-ray lightcurves photons using our CML criterion can be found in Supporting Information S1 (Figures S1 and S2).

3.2. Visibility and Distribution of Auroral Photons Across the X-Ray Auroral Structures

The tilt of Jupiter, as viewed from the observer, can lead to issues of viewing geometry of the planet when using remote sensing data (e.g., Dunn et al., 2017, 2020a; Weigt et al., 2021c). As the magnetic field at the South pole is more dipolar, this tilt of the planet affects these emissions the most when viewed from Earth. However we cannot completely neglect such effects when viewing the northern emissions as the longitude of the observer (or CML) can change what parts of the emissions are observed. To resolve such issues, we utilize the higher spatial resolution of the HST-STIS instrument compared to Chandra to model the visibility of each X-ray auroral structure, using the area of the region defined in SIII lon and lat as they rotate into view of HST-STIS. We use the number of visible pixels of each X-ray region as it rotates into view as a proxy to gauge the visibility of our X-ray structures as viewed by an observer at Earth. In other words, we analyze how much of an effect the tilt of the planet has when observing fixed regions (in SIII lon and lat) on Jupiter from any Earth-based instrument. We define the visibility here as the number of visible STIS pixels associated with each X-ray region during one Jovian rotation. We assume that the emissions across the area of the defined X-ray structures used in the model were uniform.

We adopt the method of Nichols et al. (2009) used to measure the visibility (as a function of normalized power) of different isolated components of UV auroral emissions during two HST campaigns in 2007, using the Advanced Camera for Surveys Solar Blind Channel. Here we apply this algorithm to the X-ray structures, using the ionospheric position and size of each region as viewed by HST-STIS (with greater resolution than Chandra). Full results and accompanying explanation of our visibility modeling over a full Jovian rotation (e.g., full CML coverage) are given in Figure S3 and Text S3 in Supporting Information S1 for the highest (orange: −3.39°) and lowest (black: −1.52°) sub-Earth latitude during the Juno main mission for all X-ray auroral structures. The sub-Earth latitude relates to how tilted Jupiter is away from the observer, resulting in the peak for both cases being different. Here, we define the visibility as the number of pixels visible for each of the X-ray regions normalized to the maximum for the lowest planetary tilt case. The CML range (110°–220°) used throughout this study is also overplotted in light-blue. The key results from our visibility modeling can be summarized as follows: (a) our choice of CML range envelopes the optimum visibility of all structures and (b) as expected, varying latitude and longitude of the X-ray regions lead to different peak CML and how they are affected by planetary tilt.

The distributions of auroral X-ray photons within each of the auroral structures for each Chandra observation are shown as a stacked bar chart in Figure 2, with the ObsIDs in order of observation start date (as shown in Table 1) throughout the duration of Juno's main mission. Each region is represented by the same colors and labels used in Figure 1 with all four examples indicated by a black arrow. The mean number of total auroral photons populating the X-ray structures, μ, is given by a horizontal dashed line with a value 92.92%. In other words, ∼93% of northern X-ray auroral emissions are likely to be located within the described X-ray regions. Observations where the sum of the components are <100%, as shown in Figure 2, indicate that concentrated emissions were also mapped to regions outside the X-ray auroral structures. The X-ray emissions used in the stacked bar chart,

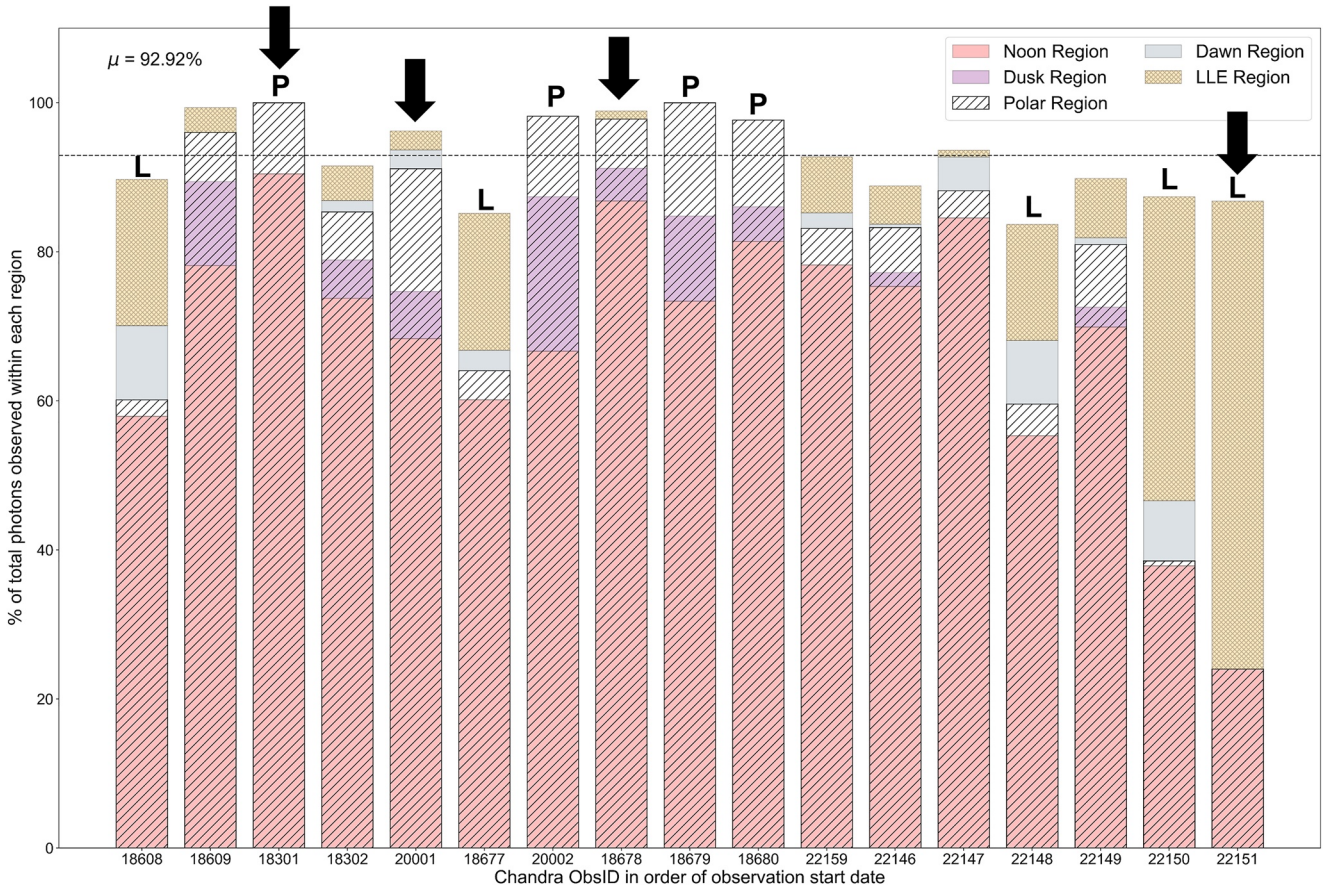

Figure 2. Stacked bar chart showing the distribution of all concentrated X-ray auroral emissions in each structure across the Juno-era Chandra observations (in order of date: Table 1), within the central meridian longitude range. Each structure in both panels are labeled with identical coloring used in Figure 1. The mean, μ, is given and indicated by the horizontal line. The letters "P" and "L" above the bars indicate auroral morphologies that fall into either the "fully polar emissions" or "low latitude emissions" categories respectively, as defined in the text. The examples shown in Figure 1 are highlighted by black arrows.

and mapped using the 2D histogram in Figure 1, span the same CML interval (110°–220°) including the peak visibility of all regions. As many of the X-ray observations have different exposure times, this ensures we are removing any observation bias as the same portion of all northern auroral emissions is observed in each of the Chandra campaigns.

As shown by the highlighted example (introduced in Figure 1a: ObsID 18301) in Figure 2 and three other observations (ObsID 20002 (no HST intervals during this time), 18679 and 18680; details of the observations in Table 1), ≥95% of concentrated northern auroral emissions are located within the X-ray polar region, and are dominated by X-ray noon photons. During these intervals there were no dawn or LLE region photons detected despite these regions being in view of Chandra at the time. However, many other observations have auroral photons located in this range within the same viewing and timing restraints. This therefore suggests that the potential drivers that cause emissions in these regions may be "switched off." Further evidence of this is shown by the observations that had a higher population of LLE photons (>10% of total photons) with no X-ray dusk emissions (ObsID 18608, 18677, 22148, 22150 and 22151). This suggests that during these intervals, the concentrated X-ray emissions were located equatorward of the ME and displaying more extreme morphological behavior when compared to the averaged map of northern auroral emissions (Weigt et al., 2021c) and there was little activity in the magnetotail. This is shown by the low occurrence rate of the X-ray emissions (using the same SIII lon/lat binning). The most extreme example, ObsID 22151 (8 September 2019: Figure 1b), is a very rare case of the majority of the auroral emissions mapping to beyond the polar region. Examples where the auroral emissions span the LLE and X-ray dusk regions (e.g., 18609, 18678, 22149) and an additional smaller population at X-ray dawn (20001, 18302, 22159) highlight possible elongation of the auroral emissions in both poleward and equatorward directions; and/

or possible X-ray emissions associated with UV injections and increased tail activity due to reconnection and other means of plasma transport (i.e., releasing of plasmoids Vogt et al., 2014).

From Figure 2, we can pick out two categories: (a) fully polar emissions (i.e., X-ray polar population ≥95% of all auroral emissions) and (b) low latitude emissions (i.e., LLE photon population >10%). These observations are labeled with "P" and "L" for both categories respectively. The observations that exhibit intermediate behavior between both categories (i.e., no "P" or "L" label) may imply a time-dependent relationship and therefore a link between the two. We do however need to compare the mapping of these morphologies with HST and Juno data to verify such a state. The key result we present here is the lack of uniformity across Figure 2 which shows that different regions can dominate when observing the northern concentrated X-ray auroral emissions. Adding a magnetospheric context this may suggest either that: (a) the switching on/off of potential magnetospheric drivers is likely to dominate or (b) the regions where conditions are right for wave growth (i.e., standing Alfvén waves and/or EMIC waves on the magnetopause boundary) is changing. This is emphasized in Figure S4 in Supporting Information S1 which shows scatter plots of photons observed in the polar region versus the LLE region and both regions plotted against inferred solar wind conditions from the Tao et al. (2005) model. As reflected in Figure 2, we observe an anticorrelation between photons populating the polar and LLE regions. There is no clear link between solar wind dynamic pressure and these populations. This may indicate that either disturbances from the solar wind are observed in multiple regions and/or the LLE region "switching on" is not directly linked to the compression and may lag ahead/behind the disturbance (i.e., similar to *i*/*I*-family).

When comparing Table 1 to Figure 2 (and Figure S4 in Supporting Information S1), there are many cases where low latitude morphologies are observed during intervals of the UV auroral emissions exhibiting either quiet (*Q*) or unsettled (*U*) conditions (ObsID 18608, 22148). This reinforces the idea of the LLE region being related to activity in the middle magnetosphere independent of the solar wind conditions (e.g., active particle injections). One other possible generation mechanism may be related to flux tubes connected to Jupiter's moons (in particular Ganymede and Io) due to the location of the LLE. Despite many of the Galilean moons observed to generate X-rays mainly from electron bremsstrahlung processes (with some contributions from particle induced X-ray emissions) from the Galileo mission (Nulsen et al., 2020), their associated X-ray auroral signatures have yet to be discovered. Therefore the LLE region may provide avenue to observe these emissions for the first time in future campaigns. Further exploration into this is beyond the scope of this work although we hope our results will highlight key examples to use in future case studies.

3.3. Using In Situ and Remote Sensing Diagnostics to Infer Magnetospheric State

In order to understand the state of the Jovian magnetosphere during the Chandra interval and constrain the driver(s) responsible for variable X-ray aurora, we combine predicted solar wind conditions from the 1D MHD propagation model by Tao et al. (2005) with data from the Juno fluxgate magnetometer (Juno MAG) and the radio and plasma wave instrument (Juno Waves). The purpose of the model is to infer how solar wind conditions can cause the Jovian magnetosphere to contract and/or expand. We can therefore infer the state of the Jovian magnetosphere, within an error of 2 days centered on the Chandra observation based on the alignment of the Sun, Earth and Jupiter. We also compare the predicted UV auroral families during the interval to the Juno data to verify the auroral behavior and morphology. The aim here is to combine the UV and X-ray predicted morphologies with observed solar wind conditions to progress the use of including X-ray spatial morphology, with the more extensively researched UV auroral morphology, as a possible proxy for magnetospheric conditions when there is no upstream in situ data. The CML constraint we employ here will allow us to find any signatures related to changing solar wind conditions and/or magnetospheric state which are still present after a few hours, such as compression events (e.g., Feng et al., 2022; Yao et al., 2022). Where possible we confirm any changing magnetospheric conditions, as carried out by previous studies (e.g., Collier et al., 2020; Hospodarsky et al., 2017; Louis et al., 2023), using Juno crossings of magnetospheric boundaries.

3.3.1. Juno Apojove Case: 16 June 2017

Figure 3 shows the results of the Tao et al. (2005) 1D MHD solar wind propagation model combined with calibrated data from Juno MAG (Connerney, 2017) and Waves (Kurth & Piker, 2022), covering 4 days centered on the Chandra (CXO) observation (shaded in orange) taken on 16 June 2017 (ObsID 20001—see Table 1 and Figure 1c). The propagation model predicted many intervals where the solar wind dynamic pressure (P_{dyn}) was

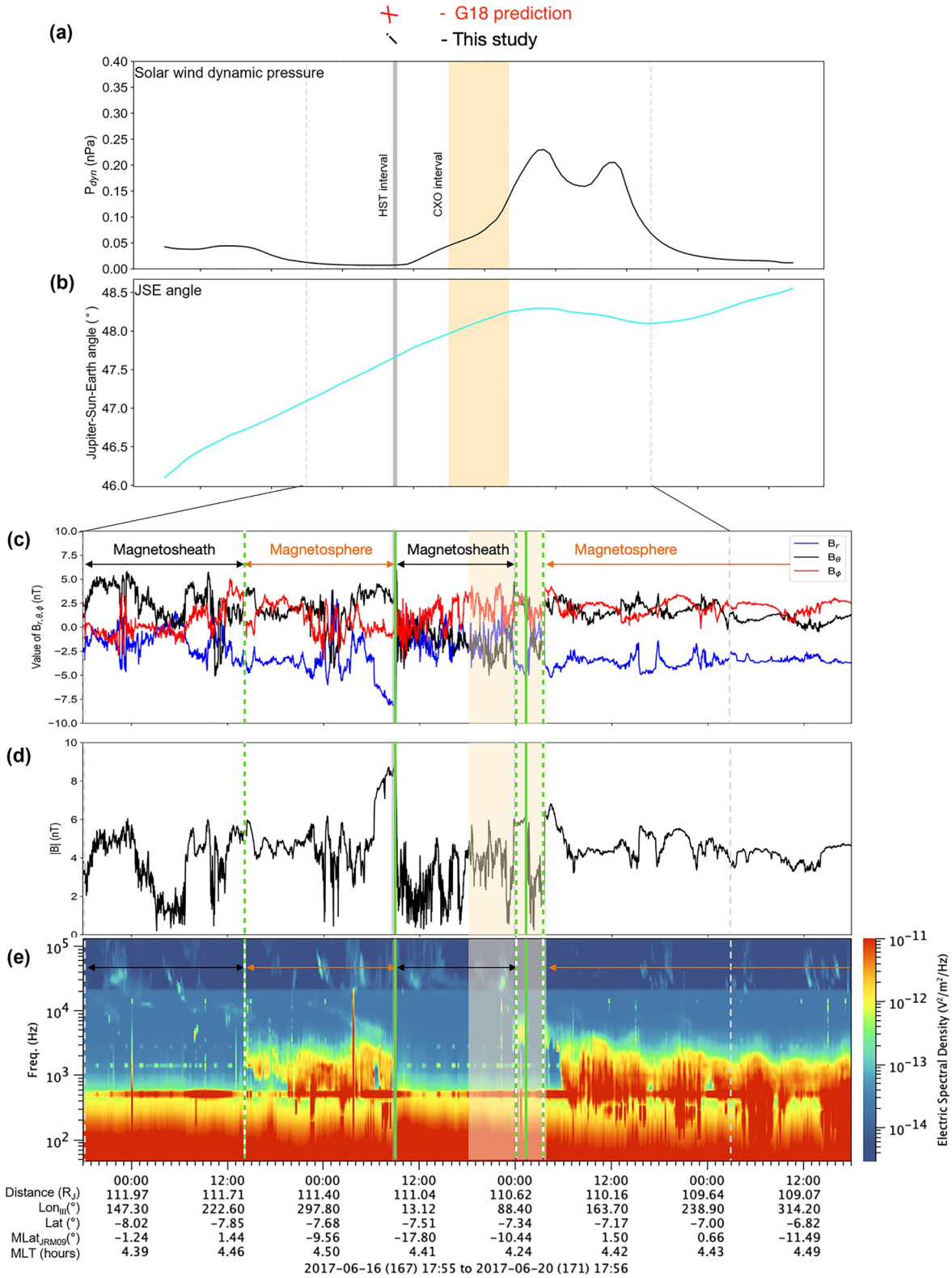

Figure 3.

increased when acting on the Jovian magnetosphere within model error, during a relatively reasonable JSE alignment (panels (a) and (b)). We only consider JSE angles <|60°| (highlighted in cyan) to ensure that the errors of the model are within the 2 days window, centered on the CXO interval. This conservative angle range allows us to explore of the Chandra catalog, and compare how the model performs with real in situ data. The HST observation is shown by the gray interval. Both CXO and HST observations lie within the 2 days window accounting for errors in the Tao et al. (2005) model (gray dashed lines). This example was selected as this Chandra interval and Juno particle data were previously analyzed by Weigt et al. (2020) to identify magnetopause crossings to infer a dynamic pressure from the Joy et al. (2002) model. When compared to the distributions of solar wind dynamic pressure (P_{dyn}) identified by Jackman and Arridge (2011) from upstream solar wind data at Jupiter spanning 1973 to 2004, both the Tao model and Juno data find the Jovian magnetosphere to be compressed during this time (P_{dyn} = ~0.23–0.39 nPa). These values lie at the upper tail of the distribution where the typical P_{dyn} observed from spacecraft data was 0.04 nPa.

The two pairs of inbound (green-white dashed vertical line) and outbound (green solid vertical line) magnetopause crossings made by Juno identified by Weigt et al. (2020) from JADE data are confirmed in the other Juno data sets (as shown in panels (c)–(e)) with a sharp discontinuity in the total magnetic field strength (|B|), in units of nanotesla (nT), and its spherical components (B_r: blue, B_θ: black, B_ϕ: red). The character of the magnetic field also changes during a crossing as it is noisier in the magnetosheath than in the magnetosphere. This is evident in Figure S5 in Supporting Information S1 (same format as Figure 3) which shows how we can use the magnetic field to delineate magnetosphere and magnetosheath using the fluctuations in |B|. Extended intervals where the fluctuations are very small (or ~0 nT) suggest Juno is in the quiet magnetospheric field. Regions where the fluctuations are significant and highly variable suggest Juno is in the noisier magnetosheath plasma.

As analyzed in the latest Juno magnetopause crossing list (up to and including Juno's ongoing Extended Mission with crossings detected June 2022), a change in B_r with a simultaneous increase in |B| prior to the magnetopause crossing (i.e., a "ramp" increase of |B|, beginning ~3–4 hr prior Juno's first outbound crossing) is a strong indicator of a compression event impacting the Jovian magnetosphere (Louis et al., 2023). Also, the two pairs of crossings identified in Figure 3 are separated by ~15-hr (i.e., >one Jovian rotation) as Juno is traveling inbound toward Jupiter from ~112 R_J (close to apogee). This suggests that the magnetopause boundary passed Juno during this time as it was moving closer to the planet, opposed to typical relaxed motion of the magnetopause under quiet or normal solar wind conditions.

The intervals where Juno crosses the magnetopause boundary and enters different regions of the magnetosphere (labeled with orange and black arrows) are also observed in the Waves data (panel (e); color bar showing the electric spectral density of the radio emissions), in particular the appearance/disappearance of the non-thermal trapped continuum emissions (as conducted by Hospodarsky et al. (2017)). These emissions, observed between the electron plasma frequency and ~10 kHz, are located in the Jovian magnetospheric cavity where the emission frequency exceeds that of the surrounding plasma frequency (e.g., Gurnett & Scarf, 1983). When in the magnetosheath, the trapped continuum emissions are blocked by the denser sheath plasma. These emissions appear again when Juno enters the more rarefied magnetospheric plasma. These transitions in electric spectral density also align with the identified Juno crossings. Signatures of a compression event are observed by the activation of broadband kilometric (bKOM) auroral radio emissions (therefore not induced by Jupiter-Galilean moon interactions) at frequencies >20 kHz (Louarn et al., 1998; Louis et al., 2023). The emissions are found to be almost continuous (i.e., almost all longitudes) and with an increased intensity during the sudden increase of |B| (and change in B_r) before the first outbound crossing, as observed by many compression events cataloged by Louis et al. (2023). The bKOM emissions have been observed

Figure 3. Multi-paneled plot combining the results from the Tao et al. (2005) 1D magnetohydrodynamic solar wind propagation model with Juno MAG and Waves, covering 4 days centering the Chandra observation (orange area) taken on 16 June 2017 (Observation ID 20001—see Table 1 for more details). Panels (a) and (b) show the predicted solar wind dynamic pressure (P_{dyn}) and associated Jupiter-Sun-Earth (JSE) angle respectively, evolving over time with the Chandra (CXO) and Hubble Space Telescope (HST) observing intervals (gray area) shown in all panels. The angle represented in cyan shows periods of time when the value is <|60°|. Panels (c) and (d) show the Juno MAG in spherical components (B_r: blue, B_θ: black, B_ϕ: red) and the total field strength (|B|) measured by the Juno MAG data, in units of nanotesla (nT), within the Tao uncertainty window used in our analysis (dashed gray vertical lines: shown in all panels). Panel (e) shows the concurrent Juno Waves data, measuring the electric spectral density of the radio and plasma wave emissions. The Juno ephemeris data during this interval is displayed at the bottom, showing its position in Jupiter's System III frame (in radial distance from Jupiter, R_J, and magnetic local time [MLT; hours]) and its position projected onto Jupiter's surface (SIII lon [Lon_{III}; degrees], SIII lat [Lat; degrees] and magnetic latitude found from the JRM09 field model [$MLat_{JRM09}$; degrees]). The green-white dashed and solid green vertical lines represent Juno making inbound and outbound crossings of the magnetopause boundary respectively, as identified from Juno JADE data as described in Weigt et al. (2020). Juno's known position in the magnetosheath (black arrows) and magnetosphere (orange arrows) are also labeled. The identified ultraviolet auroral family using the Grodent et al. (2018) definitions from G18 (red) and this study (black), as shown in Table 1, are at the top of panel (a).

to be strongly modulated by solar wind conditions rather than rotation (i.e., emissions originate from sources more active in a given Local Time region as opposed to being fixed in Jovian longitude; Zarka et al., 2021).

Finally, during the series of compressions Grodent et al. (2018) found that the UV auroral emissions exhibited features associated with the *X*-family (red label above panel (a)), suggesting that the magnetosphere was being affected by a solar wind compression region likely leading to UV main auroral brightening (MABs; Yao et al., 2022). When comparing these results to Figure 2, the X-ray auroral emissions spans across multiple regions and are dominated by X-ray noon. We identify this morphology to likely be associated with the *i*-family (black label) or moderate injections which often occur after an external perturbation (see G18). The X-ray morphology is observed to be between our defined categories and agree with Weigt et al. (2020) who observe the northern auroral emissions to be more extended and map to the dayside magnetopause boundary, along the noon-dusk sector using the Vogt et al. (2011, 2015) flux equivalence model. This may therefore suggest that, in this case, the auroral morphology reflects a magnetosphere disturbed in multiple regions and the emissions likely remain poleward and more concentrated during intervals of compressions. This example was used as a "proof of concept" of compression identification as the location of Juno was near its apojove position and allowed us to sample the conditions of the magnetopause environment.

We now extend this analysis to a case where Juno's position makes it difficult to decipher any signatures of solar wind changes; the plasmasheet approaching Juno's perigee (or perijove). Here, we begin to progress using the properties of X-ray and UV morphologies together as a possible proxy and show how this may lead to the beginning of using X-ray emissions as a diagnostic of magnetospheric response.

3.3.2. Juno Perijove Case: 1 April 2018

Figure 4 shows an example when Juno is near perijove during the Chandra interval on 1 April 2018 (ObsID 18678—see Table 1 and Figure 1d), making it difficult to infer the state of the magnetosphere due to the very strong field strength as Juno approaches Jupiter (panels (a) through (c)). Juno made several plasmasheet crossings prior to the CXO interval as shown by the sharp transition in electric spectral density, where the denser plasmasheet blocks the continuum emissions via refraction effects (analogous to the case of magnetopause crossings). Intervals when Juno is inside the plasmasheet are indicated by pink arrows. From this position we have limited ability from the in situ measurements to infer the upstream conditions, unlike at apojove when magnetopause boundary crossings can give us snapshots of magnetospheric size and inferred upstream dynamic pressure.

During Juno's approach to perijove, the current sheet model developed by Connerney et al. (2020) reported notably weak parameters associated with the middle magnetosphere from ~50–10 R_J. This is consistent with the abnormally weak plasma densities later reported by Huscher et al. (2021) in the current sheet, both suggesting that the magnetospheric conditions were quiet during Juno's inbound approach. Therefore the expectation, from these Juno inbound results 12+ hours before our CXO and HST observations, is that the magnetosphere should be quiet during perijove. However, the Tao et al. (2005) model suggests that during this time there is a series of solar wind compressions during the Juno perijove interval, with a maximum dynamic pressure of ~0.28 nPa (see Table 1). The JSE angle was within the <|60°| constraint for most of the 2 days interval, and therefore on the limit of feasibility and reliability of the propagation model. We therefore rely slightly more on the UV and X-ray morphologies in this case to observe the magnetospheric dynamics.

At the beginning of this interval the solar wind dynamic pressure is found to increase as the magnetic field in the inner/middle magnetosphere is found to reconfigure, as shown by a possible dipolarization of the field (30 March, 12:25–13:00; panels (a) through (c) in Figure 4). A dipolarization signature is observed when the magnetic field line which Juno travels across changes from a stretched to a more dipolar configuration in the middle magnetosphere (see panel (c), interval marked with vertical black lines). As a result, this can lead to a sharp decrease in B_r and simultaneous increase in B_θ linked to magnetospheric current redistribution and reconfiguration of the magnetic field (e.g., Louarn et al., 2014; Yao et al., 2020) and, for the case of the magnetotail, leads to the formation and release of a plasmoid downtail (e.g., Kronberg et al., 2005; Russell et al., 1998; Vogt et al., 2010). Such dipolarizations of the field in the middle magnetosphere have been found to be associated with injection events found from HST UV observations and can be accompanied by bright dawn storm emissions (Yao et al., 2020). These bright dawn storm emissions have been found to be correlated with a brightening of HXR intensity in the Jovian aurora (Wibisono et al., 2021), likely linked to similar regions of electron bremsstrahlung activity (e.g., Branduardi-Raymont et al., 2008). However, we note that the CXO interval was 2–3 Jovian rotations after the reconfiguration of the field and showed no concentrated X-ray emissions in expected the dawn or LLE regions. Therefore it is unlikely that the X-ray morphology will reflect this behavior.

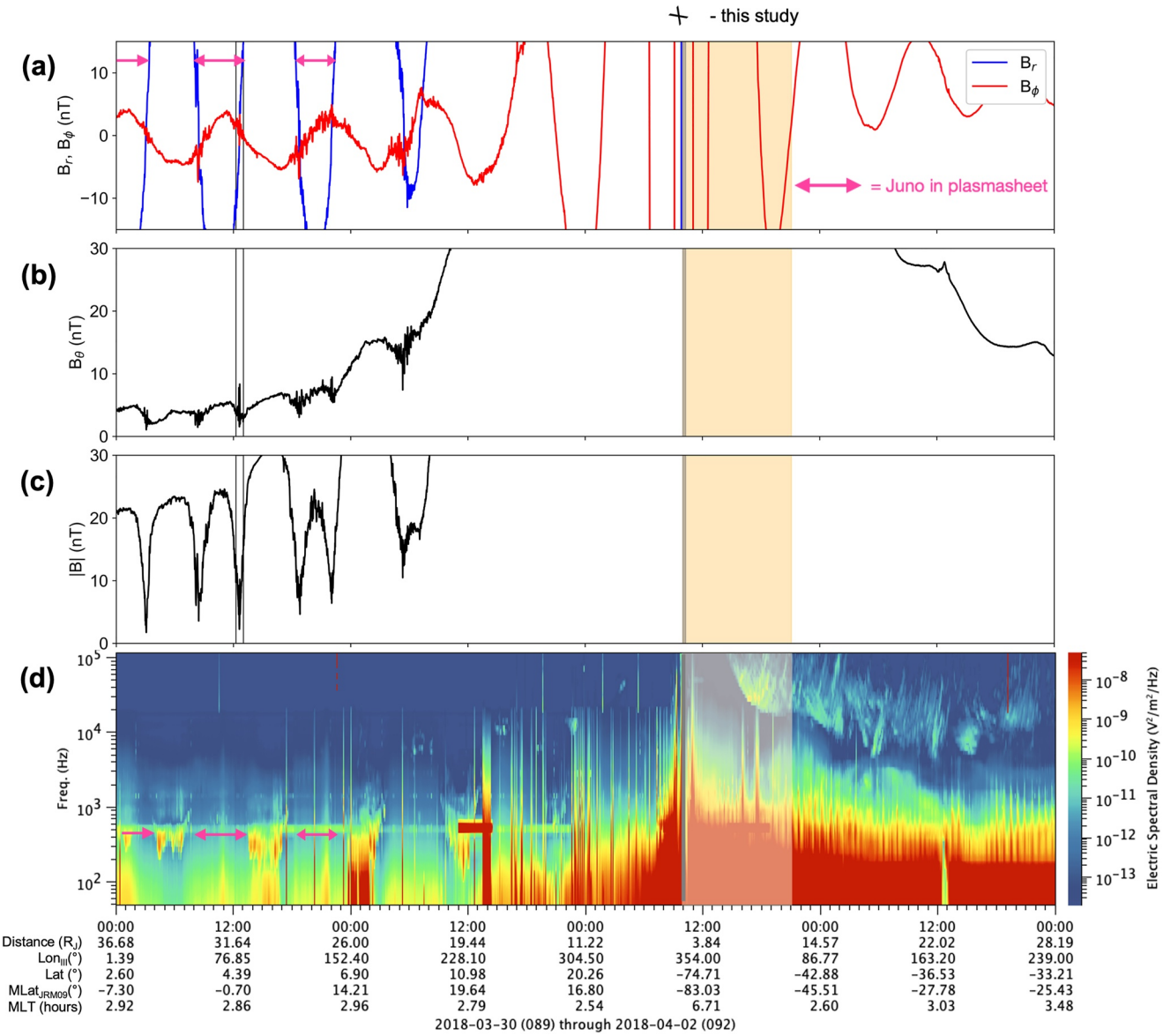

Figure 4. Multi-paneled plot for Observation ID 18678 (1 April 2018; at Juno perigee or perijove) in identical format to final three panels of Figure 3, with B_θ separated from the other components (panel (b)). CXO and Hubble Space Telescope interval are highlighted in orange and gray respectively. Black vertical lines in field data indicate interval containing a possible solar wind induced dipolarization (30 March, 12:15–13:00). As explained in text, Tao et al. (2005) model predicts a solar wind compression during the Juno interval, with $P_{dyn} = 0.28$ nPa, within the model errors (as explained for Figure 3). The Grodent et al. (2018) ultraviolet family identified in this study, *X*, is shown at the top of panel (a). Intervals when Juno is in the plasmasheet prior to perijove (identified by Juno data sets) are shown with pink arrows.

In panel (d), the spectrogram contains a variety of identifiable features including: periodic emissions (up to ∼1–100 kHz as bursts of high electric spectral density); bKOM emissions in highest frequency channels (i.e., a possible proxy to solar wind compressions; Louis et al., 2023), notably during the CXO observation and the aforementioned continuum emissions, used as indicator of plasmasheet crossings. Juno Waves also observes increased activity during perijove suggesting the magnetosphere is no longer in the quiet state identified by Connerney et al. (2020) and Huscher et al. (2021), and in agreement with the increased solar wind dynamic pressure. Although since Juno is at perijove, it is difficult to disentangle sources associated with the state of the Jovian magnetosphere and verify the model results. Signatures of the magnetosphere being disturbed just after perijove are also observed from the UV auroral emissions. Here, we identify that the UV auroral emissions are associated with the *X*-family,

agreeing with the predicted model results, coinciding with the start of the CXO interval. Therefore it is likely that the observed X-ray auroral morphology occurred during a disturbed state of the magnetosphere.

When comparing Figure 4 to Figure 2, the auroral emissions found in ObsID 18678 exhibited morphology in between our defined categories: the majority of emissions located in the X-ray polar region with a small portion of the emissions located in the LLE region (<10%). The small population of X-ray dusk photons indicate that the morphology extended polewards similar to ObsID 20001, and there may be increased tail activity likely driven by internal plasma transport and/or compressions of the magnetotail. Comparing Figures 1c and 1d, the auroral morphology is very similar with the exception of the dawn region. Therefore this distribution of X-ray auroral photons and UV auroral behavior may be an indicator of a disturbed magnetosphere due to a potential compression event. Furthermore, both CXO observations had UV morphologies linked to external perturbations and MABs due to solar wind compression events. We can therefore hypothesize that ObsID 18678, with similar X-ray morphology to ObsID 20001 which occurred during a confirmed compression, likely was observed during similar solar wind conditions (and therefore magnetospheric states). Identifying such disturbances may be associated with a possible injection event which may precede or follow a compression event as observed by G18.

We do note that further in depth analysis of the magnetic field and particle data is needed to confirm this, however the results provided here will likely highlight this observation (and many others associated with possible disturbances) as one of interest for further study. The Juno in situ data can provide evidence of dynamics, although if they are not concurrent with the CXO light-corrected observations it is very hard to compare shorter timescales between external and internal perturbations and their effects on spatial morphology and X-ray pulsations. Future work will focus on honing in on timescales between these features, and progress X-ray auroral emissions as a solar wind diagnostic like their UV counterpart.

4. Summary and Discussion

We present X-ray "auroral structures" mapping to various regions in the magnetosphere linking X-ray auroral morphology to magnetospheric dynamics in the Jovian system. Using CXO, HST and Juno data spanning the majority of Juno's main mission (24 May 2016 to 8 September 2019), we are able to compare observed magnetospheric dynamics to UV and X-ray remote sensing data. The results of our auroral distributions can be summarized as follows:

1. The X-ray auroral emissions show two clear categories of auroral morphological distributions: (a) fully polar aurora (b) low latitude emissions.
2. Non-uniformity of auroral distributions suggest there are likely numerous drivers responsible for the X-ray northern auroral emissions or conditions in the magnetosphere that permit the growth of drivers (i.e., EMIC waves) change.
3. We begin the progression of using UV and X-ray morphologies together as a possible proxy for solar wind conditions (particularly during compressions) to identify magnetospheric disturbances.
4. Visibility (or planetary tilt) has very little effect when observing the auroral photon distributions.
5. X-ray auroral distributions may highlight potential magnetospheric phenomena (i.e., prior injection events) for future study.

We note that only CXO observations which had a HST observation ±1 day from the Chandra window were considered for this study. For example, ObsID 20002 (6 August 2017; see full catalog in Weigt et al. (2021c)) does not appear in our study, however initial analysis of magnetopause crossings made by Juno suggest that the magnetosphere was compressed during this time using the Joy et al. (2002) model.

From the non-uniformity across the northern auroral distributions (Figure 2) and our visibility modeling of the regions, the lack of emissions we observe in a given region is more likely associated with the switching on/off of drivers. The X-ray noon population dominates the majority of observations suggesting that the likely driver from these emissions lies on the noon magnetopause boundary, as observed by Weigt et al. (2021c). Here, X-ray noon coincides with the location of the UV polar and swirl region and therefore linked to a very dynamic region of the dayside magnetosphere. Dayside drivers such as magnetic reconnection would occur more frequently on the noon magnetosphere compared to other regions, especially during periods of high P_{dyn}. In these situations the solar wind is likely to reconnect with the Jovian outer magnetosphere either at high latitudes in the cusps (Bunce

et al., 2004) or compressions may induce reconnection inside the Jovian system (i.e., at multiple smaller sites in the plasmasheet with more drizzle-like reconnection (Guo et al., 2018)).

Recent MHD numerical simulations from Feng et al. (2022) modeling auroral responses to solar wind compressions, using a non-tilted dipole Jovian field, found up-down-up trends of Birkeland currents (or field-aligned currents) and Alfvénic power (AP; calculated using the Poynting flux) mapping to the UV ME. No dipole tilt was used as it is not the main factor controlling the responses of Birkeland current and AP. With regards to this study, we focus on their simulations that look at Birkeland current and AP response 5-hr after a compression event (i.e., initial increase). Their model found an increase in total upward Birkeland currents and AP during this time, particularly in the dawn-noon region, with the Birkeland current having a more delayed response compared to AP. Such a response results from the dayside magnetosphere being compressed immediately from the shock, increasing equatorial plasma velocity shear. The delay in responses is found to be linked to local magnetospheric changes from sudden changes in magnetosphere shape, producing large amounts of AP on the magnetopause boundary (e.g., Manners & Masters, 2020), versus Birkeland currents being likely linked to the global configuration of current systems connecting the middle and outer Jovian magnetosphere. We would expect there to be similar trends with the brightness of HXRs (e.g., bremsstrahlung emissions) near the UV ME (X-ray dawn, equatorward regions of X-ray noon, LLE region) with higher upward Birkeland currents promoting more downward electron precipitation, assuming they are generated from the same electron population (e.g., Branduardi-Raymont et al., 2008). Previous HST campaigns have confirmed this may be the case for the UV aurora from observations of MABs observed at all local times after compression and possible injection events (Yao et al., 2022).

For the fully polar aurora, SXRs generated from ion precipitation originating from the outer magnetosphere may be modulated by the changes in AP. One current, and widely accepted, mechanism for connecting the SXRs to auroral dynamics observed in other wavelengths is ion precipitation governed by EMIC waves. Such waves will likely contribute to AP along the magnetopause boundary and will be greatly affected by distortions in the local magnetosphere shape (i.e., perturbing the local magnetic field) due to processes such as dayside reconnection and Kelvin-Helmholtz instabilities, occurring more frequently due to a compression. Therefore an initial increase of AP after compression may result in the initial processes of the ions being energized to the energies required for the generation of SXRs at the poles (e.g., Cravens et al., 2003; Dunn et al., 2017; Weigt et al., 2021c).

We note that previous analysis of three intervals during compression events (ObsID 20001, 20002, 18678) were found to exhibit very significant quasi-periodic oscillations (QPOs) within a region located in the center of X-ray noon (the AHSNuc). These QPOs were observed to be between 2- and 4- min suggesting very dynamic activity on the noon boundary and timescales linked to magnetic reconnection on the boundary (Weigt et al., 2021c). However, Weigt et al. (2021c) observed that time QPOs were likely to be spatial dependent and therefore the period and statistical significance changes with where you observe in the aurora. They also stated that any activity may be initiated at the noon magnetopause boundary and be advected along the magnetopause boundary toward the flanks. This may explain the non-uniformity of auroral distributions we discuss here and how wave growth is promoted in other regions of the magnetosphere such as the strong correlations between X-ray emissions and EMIC waves found in the outer dawn and midnight magnetosphere (Yao et al., 2021). Therefore, assuming the auroral emissions are generated from wave activity, the changing auroral morphology may reveal the propensity for wave activity in different components in the Jovian magnetosphere.

The peak visibility of each X-ray auroral structure was within our CML threshold throughout the Juno era during with changing sub-Earth latitudes mainly affecting those regions nearest to the pole (i.e., X-ray dusk). We do note however that the changing sub-Earth latitudes will have the greatest effect in the southern auroral region. Therefore future studies will need to develop a new set of X-ray auroral structures to combat this effect. The techniques discussed in this study can be extended to the southern auroral region and will allow detailed exploration and comparisons between both auroral regions (i.e., North-South asymmetry and non-conjugacy observed in the auroral X-ray emissions Branduardi-Raymont et al. (2004), Jackman et al. (2018), Mori et al. (2022), and Weigt et al. (2021c) and other wavelengths). This has already been shown by Mori et al. (2022) for HXRs, where non-thermal bremsstrahlung X-rays were ∼twice as bright in the southern auroral region than the North, consistent with more persistent and stronger electron currents than those observed in the North (Kotsiaros et al., 2019).

In order to fully categorize the Jovian X-ray auroral emissions and the extent of the solar wind influence at both poles, current X-ray technology needs to be expanded upon. Future potential missions such as Lynx (Falcone et al., 2019) and Line Emission Mapper (LEM; Kraft et al., 2022) will allow us to explore in detail the various drivers generating X-ray emissions in the Jovian magnetosphere. Utilizing the enhanced spectral resolution that is, 1–2 eV spectral resolution in the 0.2–2 keV range for LEM) and greater effective area at lower energies, we will be able to delve into the softer X-ray spectrum and evaluate the ion populations dominating various X-ray processes (e.g., charge exchange) and eventually including the southern hemisphere. Coupling these remote sensing instruments with data from an in situ X-ray probe (Dunn et al., 2023) will be the key to fully understanding the magnetospheric drivers responsible for the Jovian auroral X-ray emissions.

Data Availability Statement

This research has made use of data obtained from the *Chandra Data Archive* and *Chandra Source Catalog* (https://cda.harvard.edu/chaser/); Juno Waves and MAG from the *NASA Planetary Data System* and solar wind data obtained via AMDA (http://amda.cdpp.eu/). Waves survey data are provided by Kurth and Piker (2022). Juno fluxgate magnetometer data are provided by Connerney (2017). The catalog of Chandra data required to reproduce the results shown in this study are stored in the Zenodo repository created by Weigt et al. (2021b). All new data products created in this study and used in both main text and Supporting Information S1 are found in Weigt et al. (2023).

Acknowledgments
DMW is supported by the Science and Technology Facilities Council (STFC) studentship ST/S505705/1 and long term attachment grant to work at the Dublin Institute for Advanced Studies (DIAS). DMW's work at DIAS is funded by European Union's Horizon 2020 research and innovation programme under grant agreement No. 952439 and project number AO 2-1927/22/NL/GLC/ov as part of the ESA OSIP Nanosats for Spaceweather Campaign. DMW's work at Trinity College Dublin is supported by Air Force Office of Scientific Research award FA9550-19-1-7010. DMP is supported by a LUFST studentship. SVB is supported by STFC projects ST/M005534/1 and ST/V000748/1. CMJ, CKL and SCMcE work at DIAS is supported by the Science Foundation Ireland (SFI) Grant 18/FRL/6199. WRD was supported by Ernest Rutherford Fellowship: ST/W003449/1. MFV was supported by NASA Grant 80NSSC20K0559. CT acknowledges support by JSPS KAKENHI 20KK0074. The research at the University of Iowa is supported by NASA through Contract 699041X with Southwest Research Institute.

References

Badman, S. V., Branduardi-Raymont, G., Galand, M., Hess, S. L. G., Krupp, N., Lamy, L., et al. (2015). Auroral processes at the giant planets: Energy deposition, emission mechanisms, morphology and spectra. *Space Science Reviews*, *187*(1–4), 99–179. https://doi.org/10.1007/s11214-014-0042-x

Ballester, G. E., Clarke, J. T., Trauger, J. T., Harris, W. M., Stapelfeldt, K. R., Crisp, D., et al. (1996). Time-resolved observations of Jupiter's far-ultraviolet aurora. *Science*, *274*(5286), 409–413. https://doi.org/10.1126/science.274.5286.409

Bolton, S. J., Lunine, J., Stevenson, D., Connerney, J. E. P., Levin, S., Owen, T. C., et al. (2017). The Juno Mission. *Space Science Reviews*, *213*(1–4), 5–37. https://doi.org/10.1007/s11214-017-0429-6

Bonfond, B., Saur, J., Grodent, D., Badman, S. V., Bisikalo, D., Shematovich, V., et al. (2017). The tails of the satellite auroral footprints at Jupiter. *Journal of Geophysical Research: Space Physics*, *122*(8), 7985–7996. https://doi.org/10.1002/2017JA024370

Bonfond, B., Yao, Z. H., Gladstone, G. R., Grodent, D., Gérard, J., Matar, J., et al. (2021). Are dawn storms Jupiter's auroral substorms? *AGU Advances*, *2*(1), 1–14. https://doi.org/10.1029/2020av000275

Branduardi-Raymont, G., Elsner, R. F., Galand, M., Grodent, D., Cravens, T. E., Ford, P., et al. (2008). Spectral morphology of the X-ray emission from Jupiter's aurorae. *Journal of Geophysical Research*, *113*(2), 1–11. https://doi.org/10.1029/2007JA012600

Branduardi-Raymont, G., Elsner, R. F., Gladstone, G. R., Ramsay, G., Rodriguez, P., Soria, R., & Waite, J. H. (2004). First observation of Jupiter by XMM-Newton. *Astronomy*, *337*(1149), 331–337. https://doi.org/10.1051/0004-6361

Bunce, E. J., Cowley, S. W., & Yeoman, T. K. (2004). Jovian cusp processes: Implications for the polar aurora. *Journal of Geophysical Research*, *109*(A9), 1–26. https://doi.org/10.1029/2003JA010280

Collier, M. R., Gruesbeck, J. R., Connerney, J. E. P., Joy, S. P., Hospodarsky, G. B., Roberts, A., et al. (2020). A K-means clustering analysis of the Jovian and terrestrial magnetopauses: A technique to classify global magnetospheric behavior. *Journal of Geophysical Research: Planets*, *125*(9), e06366. https://doi.org/10.1029/2019JE006366

Connerney, J. E. P. (2017). Juno fluxgate magnetometer calibrated data v1.0 [Dataset]. NASA Planetary Data System. https://doi.org/10.17189/1519711

Connerney, J. E. P., Benn, M., Bjarno, J. B., Denver, T., Espley, J., Jorgensen, J. L., et al. (2017). The Juno magnetic field investigation. *Space Science Reviews*, *213*(1–4), 39–138. https://doi.org/10.1007/s11214-017-0334-z

Connerney, J. E. P., Timmins, S., Herceg, M., & Joergensen, J. L. (2020). A Jovian magnetodisc model for the Juno era. *Journal of Geophysical Research: Space Physics*, *125*(10), e2020JA028138. https://doi.org/10.1029/2020JA028138

Connerney, J. E. P., Timmins, S., Oliversen, R. J., Espley, J. R., Joergensen, J. L., Kotsiaros, S., et al. (2022). A new model of Jupiter's magnetic field at the completion of Juno's Prime Mission. *Journal of Geophysical Research: Planets*, *127*(2), e2021JE007055. https://doi.org/10.1029/2021JE007055

Cravens, T. E., Waite, J. H., Gombosi, T. I., Lugaz, N., Gladstone, G. R., Mauk, B. H., & MacDowall, R. J. (2003). Implications of Jovian X-ray emission for magnetosphere-ionosphere coupling. *Journal of Geophysical Research*, *108*(A12), 1–12. https://doi.org/10.1029/2003JA010050

Dumont, M., Grodent, D., Radioti, A., Bonfond, B., & Gérard, J. (2014). Jupiter's equatorward auroral features: Possible signatures of magnetospheric injections. *Journal of Geophysical Research: Space Physics*, *119*(12), A07000. https://doi.org/10.1002/2014JA020527

Dumont, M., Grodent, D., Radioti, A., Bonfond, B., Roussos, E., & Paranicas, C. (2018). Evolution of the auroral signatures of Jupiter's magnetospheric injections. *Journal of Geophysical Research: Space Physics*, *123*(2015), 1–13. https://doi.org/10.1029/2018JA025708

Dunn, W. R. (2022). X-ray emissions from the Jovian system. In C. Bambi & A. Santangelo (Eds.), *Handbook of x-ray and gamma-ray astrophysics* (p. 110). https://doi.org/10.1007/978-981-16-4544-0_73-1

Dunn, W. R., Berland, G., Roussos, E., Clark, G., Kollmann, P., Turner, D., et al. (2023). Exploring fundamental particle acceleration and loss processes in heliophysics through an orbiting X-ray instrument in the Jovian system. *arXiv e-prints*. arXiv:2303.02161. https://doi.org/10.48550/arXiv.2303.02161

Dunn, W. R., Branduardi-Raymont, G., Carter-Cortez, V., Campbell, A., Elsner, R., Ness, J.-U., et al. (2020a). Jupiter's X-ray emission during the 2007 solar minimum. *Journal of Geophysical Research: Space Physics*, *125*(6), e2019JA027219. https://doi.org/10.1029/2019JA027219

Dunn, W. R., Branduardi-Raymont, G., Elsner, R. F., Vogt, M. F., Lamy, L., Ford, P. G., et al. (2016). The impact of an ICME on the Jovian X-ray aurora. *Journal of Geophysical Research A: Space Physics*, *121*(3), 2274–2307. https://doi.org/10.1002/2015JA021888

Dunn, W. R., Branduardi-Raymont, G., Ray, L. C., Jackman, C. M., Kraft, R. P., Elsner, R. F., et al. (2017). The independent pulsations of Jupiter's northern and southern X-ray auroras. *Nature Astronomy*, *1*(11), 758–764. https://doi.org/10.1038/s41550-017-0262-6

Dunn, W. R., Gray, R., Wibisono, A. D., Lamy, L., Louis, C., Badman, S. V., et al. (2020b). Comparisons between Jupiter's X-ray, UV and radio emissions and in-situ solar wind measurements during 2007. *Journal of Geophysical Research: Space Physics*, *125*(6), e2019JA027222. https://doi.org/10.1029/2019JA027222

Dunn, W. R., Weigt, D. M., Grodent, D., Yao, Z. H., May, D., Feigelman, K., et al. (2022). Jupiter's X-ray and UV dark polar region. *Geophysical Research Letters*, *4*(11), e2021GL097390. https://doi.org/10.1029/2021GL097390

Elsner, R. F., Lugaz, N., Waite, J. H., Cravens, T. E., Gladstone, G. R., Ford, P., et al. (2005). Simultaneous Chandra X ray Hubble Space Telescope ultraviolet, and Ulysses radio observations of Jupiter's aurora. *Journal of Geophysical Research*, *110*(A1), 1–16. https://doi.org/10.1029/2004JA010717

Falcone, A. D., Kraft, R. P., Bautz, M. W., Gaskin, J. A., Mulqueen, J. A., & Swartz, D. A. (2019). Overview of the high-definition x-ray imager instrument on the Lynx x-ray surveyor. *Journal of Astronomical Telescopes, Instruments, and Systems*, *5*(2), 1. https://doi.org/10.1117/1.JATIS.5.2.021019

Feng, E., Zhang, B., Yao, Z., Delamere, P. A., Zheng, Z., Brambles, O. J., et al. (2022). Dynamic Jovian magnetosphere responses to enhanced solar wind ram pressure: Implications for auroral activities. *Geophysical Research Letters*, *49*(19), e2022GL099858. https://doi.org/10.1029/2022GL099858

Gerard, J. C., Grodent, D., Prange, R., Waite, J. H., Gladstone, G. R., Dols, V., et al. (1994). A remarkable auroral event on Jupiter observed in the ultraviolet with the Hubble Space Telescope. *Science*, *266*(5191), 1675–1678. https://doi.org/10.1126/science.266.5191.1675

Gray, R. L., Badman, S. V., Bonfond, B., Kimura, T., Misawa, H., Nichols, J. D., et al. (2016). Auroral evidence of radial transport at Jupiter during January 2014. *Journal of Geophysical Research: Space Physics*, *121*(10), 9972–9984. https://doi.org/10.1002/2016JA023007

Greathouse, T., Gladstone, R., Versteeg, M., Hue, V., Kammer, J., Giles, R., et al. (2021). Local time dependence of Jupiter's polar auroral emissions observed by Juno UVS. *Journal of Geophysical Research: Planets*, *126*(12), 1–13. https://doi.org/10.1029/2021JE006954

Grodent, D. (2015). A brief review of ultraviolet auroral emissions on giant planets. *Space Science Reviews*, *187*(1–4), 23–50. https://doi.org/10.1007/s11214-014-0052-8

Grodent, D., Bonfond, B., Yao, Z., Gérard, J. C., Radioti, A., Dumont, M., et al. (2018). Jupiter's aurora observed with HST during Juno orbits 3 to 7. *Journal of Geophysical Research: Space Physics*, *123*(5), 3299–3319. https://doi.org/10.1002/2017JA025046

Grodent, D., Clarke, J. T., Kim, J., Waite, J. H., & Cowley, S. W. H. (2003). Jupiter's main auroral oval observed with HST-STIS. *Journal of Geophysical Research*, *108*(A11), 1389. https://doi.org/10.1029/2003JA009921

Grodent, D., Clarke, J. T., Waite, J. H., Cowley, S. W., Gérard, J. C., & Kim, J. (2003). Jupiter's polar auroral emissions. *Journal of Geophysical Research*, *108*(A10), 1–9. https://doi.org/10.1029/2003JA010017

Guo, R. L., Yao, Z. H., Sergis, N., Wei, Y., Mitchell, D., Roussos, E., et al. (2018). Reconnection acceleration in Saturn's dayside magnetodisk: A multicase study with Cassini. *The Astrophysical Journal*, *868*(2), L23. https://doi.org/10.3847/2041-8213/aaedab

Gurnett, D. A., & Scarf, F. L. (1983). Plasma waves in the Jovian magnetosphere. In A. J. Dessler (Ed.), *Physics of the Jovian magnetosphere* (pp. 285–316). Cambridge University Press. https://doi.org/10.1017/CBO9780511564574.010

Hospodarsky, G. B., Kurth, W. S., Bolton, S. J., Allegrini, F., Clark, G. B., Connerney, J. E., et al. (2017). Jovian bow shock and magnetopause encounters by the Juno spacecraft. *Geophysical Research Letters*, *44*(10), 4506–4512. https://doi.org/10.1002/2017GL073177

Houston, S. J., Cravens, T. E., Schultz, D. R., Gharibnejad, H., Dunn, W. R., Haggerty, D. K., et al. (2020). Jovian auroral ion precipitation: X-ray production from oxygen and sulfur precipitation. *Journal of Geophysical Research: Space Physics*, *125*(2), 2019JA027007. https://doi.org/10.1029/2019JA027007

Huscher, E., Bagenal, F., Wilson, R. J., Allegrini, F., Ebert, R. W., Valek, P. W., et al. (2021). Survey of Juno observations in Jupiter's plasma disk: Density. *Journal of Geophysical Research: Space Physics*, *126*(8), e29446. https://doi.org/10.1029/2021JA029446

Jackman, C. M., & Arridge, C. S. (2011). Solar cycle effects on the dynamics of Jupiter's and Saturn's magnetospheres. *Solar Physics*, *274*(1–2), 481–502. https://doi.org/10.1007/s11207-011-9748-z

Jackman, C. M., Knigge, C., Altamirano, D., Gladstone, R., Dunn, W., Elsner, R., et al. (2018). Assessing quasi-periodicities in Jovian X-ray emissions: Techniques and heritage survey. *Journal of Geophysical Research: Space Physics*, *123*(11), 9204–9221. https://doi.org/10.1029/2018JA025490

Joy, S. P., Kivelson, M. G., Walker, R. J., Khurana, K. K., Russell, C. T., & Ogino, T. (2002). Probabilistic models of the Jovian magnetopause and bow shock locations. *Journal of Geophysical Research*, *107*(A10), 1–17. https://doi.org/10.1029/2001JA009146

Kasahara, S., Kronberg, E. A., Kimura, T., Tao, C., Badman, S. V., Masters, A., et al. (2013). Asymmetric distribution of reconnection jet fronts in the Jovian nightside magnetosphere. *Journal of Geophysical Research: Space Physics*, *118*(1), 375–384. https://doi.org/10.1029/2012JA018130

Kimura, T., Nichols, J. D., Gray, R. L., Tao, C., Murakami, G., Yamazaki, A., et al. (2017). Transient brightening of Jupiter's aurora observed by the Hisaki satellite and Hubble Space Telescope during approach phase of the Juno spacecraft. *Geophysical Research Letters*, *44*(10), 4523–4531. https://doi.org/10.1002/2017GL072912

Kotsiaros, S., Connerney, J. E., Clark, G., Allegrini, F., Gladstone, G. R., Kurth, W. S., et al. (2019). Birkeland currents in Jupiter's magnetosphere observed by the polar-orbiting Juno spacecraft. *Nature Astronomy*, *3*(10), 904–909. https://doi.org/10.1038/s41550-019-0819-7

Kraft, R., Markevitch, M., Kilbourne, C., Adams, J. S., Akamatsu, H., Ayromlou, M., et al. (2022). Line Emission Mapper (LEM): Probing the physics of cosmic ecosystems. *arXiv e-prints*. arXiv:2211.09827. https://doi.org/10.48550/arXiv.2211.09827

Kronberg, E. A., Woch, J., Krupp, N., Lagg, A., Khurana, K. K., & Glassmeier, K. H. (2005). Mass release at Jupiter: Substorm-like processes in the Jovian magnetotail. *Journal of Geophysical Research*, *110*(A3), A03211. https://doi.org/10.1029/2004JA010777

Kurth, W. S., Hospodarsky, G. B., Kirchner, D. L., Mokrzycki, B. T., Averkamp, T. F., Robison, W. T., et al. (2017). The Juno waves investigation. *Space Science Reviews*, *213*(1–4), 347–392. https://doi.org/10.1007/s11214-017-0396-y

Kurth, W. S., & Piker, C. W. (2022). Juno waves calibrated survey full resolution v2.0 [Dataset]. NASA Planetary Data System. https://doi.org/10.17189/1520498

Louarn, P., Paranicas, C. P., & Kurth, W. S. (2014). Global magnetodisk disturbances and energetic particle injections at Jupiter. *Journal of Geophysical Research: Space Physics*, *119*(6), 4495–4511. https://doi.org/10.1002/2014JA019846

Louarn, P., Roux, A., Perraut, S., Kurth, W., & Gurnett, D. (1998). A study of the large-scale dynamics of the Jovian magnetosphere using the Galileo plasma wave experiment. *Geophysical Research Letters*, *25*(15), 2905–2908. https://doi.org/10.1029/98GL01774

Louis, C. K., Jackman, C. M., Hospodarsky, G., O'Kane Hackett, A., Devon-Hurley, E., Zarka, P., et al. (2023). Effect of a magnetospheric compression on Jovian radio emissions: In situ case study using Juno data. *Journal of Geophysical Research: Space Physics*, *128*(9), e2022JA031155. https://doi.org/10.1029/2022JA031155

Manners, H., & Masters, A. (2020). The global distribution of ultra-low-frequency waves in Jupiter's magnetosphere. *Journal of Geophysical Research: Space Physics*, *125*(10), e2020JA028345. https://doi.org/10.1029/2020JA028345

McComas, D. J., Szalay, J. R., Allegrini, F., Bagenal, F., Connerney, J., Ebert, R. W., et al. (2017). Plasma environment at the dawn flank of Jupiter's magnetosphere: Juno arrives at Jupiter. *Geophysical Research Letters*, *44*(10), 4432–4438. https://doi.org/10.1002/2017GL072831

McEntee, S. C., Jackman, C. M., Weigt, D. M., Dunn, W. R., Kashyap, V., Kraft, R., et al. (2022). Comparing Jupiter's equatorial x-ray emissions with solar x-ray flux over 19 years of the Chandra mission. *Journal of Geophysical Research: Space Physics*, *127*(12), e2022JA030971. https://doi.org/10.1029/2022JA030971

Mori, K., Hailey, C., Bridges, G., Mandel, S., Garvin, A., Grefenstette, B., et al. (2022). Observation and origin of non-thermal hard X-rays from Jupiter. *Nature Astronomy*, *6*(4), 442–448. https://doi.org/10.1038/s41550-021-01594-8

Nichols, J. D., Badman, S. V., Bagenal, F., Bolton, S. J., Bonfond, B., Bunce, E. J., et al. (2017). Response of Jupiter's auroras to conditions in the interplanetary medium as measured by the Hubble Space Telescope and Juno. *Geophysical Research Letters*, *44*(15), 7643–7652. https://doi.org/10.1002/2017GL073029

Nichols, J. D., Clarke, J. T., Gérard, J. C., Grodent, D., & Hansen, K. C. (2009). Variation of different components of Jupiter's auroral emission. *Journal of Geophysical Research*, *114*(6), 1–18. https://doi.org/10.1029/2009JA014051

Nulsen, S., Kraft, R., Germain, G., Dunn, W., Tremblay, G., Beegle, L., et al. (2020). X-ray emission from Jupiter's Galilean moons: A tool for determining their surface composition and particle environment. *The Astrophysical Journal*, *895*(2), 79. https://doi.org/10.3847/1538-4357/ab8cbc

Pallier, L., & Prangé, R. (2001). More about the structure of the high latitude Jovian aurorae. *Planetary and Space Science*, *49*(10–11), 1159–1173. https://doi.org/10.1016/S0032-0633(01)00023-X

Radioti, A., Grodent, D., GéRard, J. C., Vogt, M. F., Lystrup, M., & Bonfond, B. (2011). Nightside reconnection at Jupiter: Auroral and magnetic field observations from 26 July 1998. *Journal of Geophysical Research*, *116*(A3), A03221. https://doi.org/10.1029/2010JA016200

Russell, C. T., Khurana, K. K., Huddleston, D. E., & Kivelson, M. G. (1998). Localized reconnection in the near Jovian magnetotail. *Science*, *280*(5366), 1061–1064. https://doi.org/10.1126/science.280.5366.1061

Swithenbank-Harris, B. G., Nichols, J. D., & Bunce, E. J. (2019). Jupiter's Dark Polar Region as observed by the Hubble Space Telescope during the Juno approach phase. *Journal of Geophysical Research: Space Physics*, *124*(11), 9094–9105. https://doi.org/10.1029/2019JA027306

Tao, C., Kataoka, R., Fukunishi, H., Takahashi, Y., & Yokoyama, T. (2005). Magnetic field variations in the Jovian magnetotail induced by solar wind dynamic pressure enhancements. *Journal of Geophysical Research*, *110*(A11), 1–9. https://doi.org/10.1029/2004JA010959

Vasyliūnas, V. M. (1983). Plasma distribution and flow. In A. J. Dessler (Ed.), *Physics of the Jovian magnetosphere* (pp. 395–453). Cambridge University Press. https://doi.org/10.1017/CBO9780511564574.013

Vogt, M. F., Bunce, E. J., Kivelson, M. G., Khurana, K. K., Walker, R. J., Radioti, A., et al. (2015). Magnetosphere-ionosphere mapping at Jupiter: Quantifying the effects of using different internal field models. *Journal of Geophysical Research: Space Physics*, *120*(4), 2584–2599. https://doi.org/10.1002/2014JA020729

Vogt, M. F., Jackman, C. M., Slavin, J. A., Bunce, E. J., Cowley, S. W. H., Kivelson, M. G., & Khurana, K. K. (2014). Structure and statistical properties of plasmoids in Jupiter's magnetotail. *Journal of Geophysical Research: Space Physics*, *119*(2), 821–843. https://doi.org/10.1002/2013JA019607.Received

Vogt, M. F., Kivelson, M. G., Khurana, K. K., Joy, S. P., & Walker, R. J. (2010). Reconnection and flows in the Jovian magnetotail as inferred from magnetometer observations. *Journal of Geophysical Research*, *115*(A6), A06219. https://doi.org/10.1029/2009JA015098

Vogt, M. F., Kivelson, M. G., Khurana, K. K., Walker, R. J., Bonfond, B., Grodent, D., & Radioti, A. (2011). Improved mapping of Jupiter's auroral features to magnetospheric sources. *Journal of Geophysical Research*, *116*(3), A03220. https://doi.org/10.1029/2010JA016148

Vogt, M. F., Rutala, M., Bonfond, B., Clarke, J. T., Moore, L., & Nichols, J. D. (2022). Variability of Jupiter's main auroral emission and satellite footprints observed with HST during the Galileo era. *Journal of Geophysical Research: Space Physics*, *127*(2), e2021JA030011. https://doi.org/10.1029/2021JA030011

Weigt, D. M., Dunn, W. R., Jackman, C. M., Kraft, R., Branduardi-Raymont, G., Nichols, J. D., et al. (2021a). Searching for Saturn's X-rays during a rare Jupiter magnetotail crossing using Chandra. *Monthly Notices of the Royal Astronomical Society*, *506*(1), 298–305. https://doi.org/10.1093/mnras/stab1680

Weigt, D. M., Gladstone, G. R., McEntee, S. C., Dunn, W. R., Kashyap, V. L., Jackman, C. M., et al. (2022). Chandra_x-ray_data_processing_pipeline version 1.0.2 (v1.0.2) [Computer Software]. Zenodo. https://doi.org/10.5281/zenodo.7380282

Weigt, D. M., Jackman, C. M., Dunn, W. R., Gladstone, G. R., Vogt, M. F., Wibisono, A. D., et al. (2020). Chandra observations of Jupiter's X-ray auroral emission during Juno apojove 2017. *Journal of Geophysical Research: Planets*, *125*(4), e2019JE006262. https://doi.org/10.1029/2019JE006262

Weigt, D. M., Jackman, C. M., Moral Pombo, D., Badman, S. V., Louis, C. K., Dunn, W. R., et al. (2023). Identifying the variety of Jovian X-ray auroral structures: Tying the morphology of X-ray emissions to associated magnetospheric dynamics [Dataset]. Zenodo. https://doi.org/10.5281/zenodo.8375516

Weigt, D. M., Jackman, C. M., Vogt, M. F., Manners, H., Dunn, W. R., Gladstone, G. R., et al. (2021b). Characteristics of Jupiter's X-ray auroral hot spot emissions using Chandra [Dataset]. Zenodo. https://doi.org/10.5281/zenodo.4275744

Weigt, D. M., Jackman, C. M., Vogt, M. F., Manners, H., Dunn, W. R., Gladstone, G. R., et al. (2021c). Characteristics of Jupiter's X-Ray auroral hot spot emissions using Chandra. *Journal of Geophysical Research: Space Physics*, *126*(9), e2021JA029243. https://doi.org/10.1029/2021JA029243

Weisskopf, M. C., Tananbaum, H. D., Van Speybroeck, L. P., & O'Dell, S. L. (2000). Chandra X-ray observatory (CXO): Overview. *X-Ray Optics, Instruments, and Missions III*, *4012*(July 2000), 2–16. https://doi.org/10.1117/12.391545

Wibisono, A. D., Branduardi-Raymont, G., Dunn, W. R., Kimura, T., Coates, A. J., Grodent, D., et al. (2021). Jupiter's X-ray aurora during UV dawn storms and injections as observed by XMM-Newton, Hubble, and Hisaki. *Monthly Notices of the Royal Astronomical Society*, *507*(1), 1216–1228. https://doi.org/10.1093/mnras/stab2218

Yao, Z., Bonfond, B., Clark, G., Grodent, D., Dunn, W., Vogt, M., et al. (2020). Reconnection- and dipolarization-driven auroral dawn storms and injections. *Journal of Geophysical Research: Space Physics*, *125*(8), e2019JA027663. https://doi.org/10.1029/2019JA027663

Yao, Z., Bonfond, B., Grodent, D., Chané, E., Dunn, W. R., Kurth, W. S., et al. (2022). On the relation between auroral morphologies and compression conditions of Jupiter's magnetopause: Observations from Juno and the Hubble Space Telescope. *Journal of Geophysical Research: Space Physics*, *127*(10), e2021JA029894. https://doi.org/10.1029/2021JA029894

Yao, Z., Dunn, W., Woodfield, E., Clark, G., Mauk, B., Ebert, R., et al. (2021). Revealing the source of Jupiter's x-ray auroral flares. *Science Advances*, *7*(28), eabf0851. https://doi.org/10.1126/sciadv.abf0851

Yoshioka, K., Murakami, G., Yamazaki, A., Tsuchiya, F., Kagitani, M., Sakanoi, T., et al. (2013). The extreme ultraviolet spectroscope for planetary science, EXCEED. *Planetary and Space Science*, *85*, 250–260. https://doi.org/10.1016/j.pss.2013.06.021

Zarka, P., Magalhães, F. P., Marques, M. S., Louis, C. K., Echer, E., Lamy, L., et al. (2021). Jupiter's auroral radio emissions observed by Cassini: Rotational versus solar wind control, and components identification. *Journal of Geophysical Research: Space Physics*, *126*(10), e29780. https://doi.org/10.1029/2021JA029780